

## Adventitial fibroblasts direct smooth muscle cell-state transition in pulmonary vascular disease

Slaven Crnkovic<sup>1,2,3\*</sup>, Helene Thekkekara Puthenparampil<sup>1\*</sup>, Shirin Mulch<sup>3</sup>, Valentina Biasin<sup>1,2</sup>, Nemanja Radic<sup>2</sup>, Jochen Wilhelm<sup>3</sup>, Marek Bartkuhn<sup>3</sup>, Ehsan Bonyadi Rad<sup>1</sup>, Alicja Wawrzen<sup>2</sup>, Ingrid Matzer<sup>2</sup>, Ankita Mitra<sup>4</sup>, Ryan Leib<sup>5</sup>, Bence M. Nagy<sup>1</sup>, Anita Sahu-Osen<sup>1</sup>, Francesco Valzano<sup>1</sup>, Natalie Bordag<sup>1,2</sup>, Matthias Evermann<sup>6</sup>, Konrad Hoetzenegger<sup>6</sup>, Andrea Olschewski<sup>1,2</sup>, Senka Ljubojevic-Holzer<sup>2</sup>, Małgorzata Wygrecka<sup>3</sup>, Kurt Stenmark<sup>7</sup>, Leigh M. Marsh<sup>1,2</sup>, Vinicio de Jesus Perez<sup>4\*</sup>, Grazyna Kwapiszewska<sup>1,2,3\*</sup>

<sup>1</sup>Ludwig Boltzmann Institute for Lung Vascular Research, Graz, Austria. <sup>2</sup>Medical University of Graz, Lung research Cluster, Graz, Austria. <sup>3</sup>Institute for Lung Health, Cardiopulmonary Institute, Member of the German Center for Lung Research, Justus-Liebig University Giessen, Giessen, Germany. <sup>4</sup>Department of Medicine and <sup>5</sup>Mass Spectrometry Laboratory, Stanford University School of Medicine, Stanford, California, United States. <sup>6</sup>Medical University of Vienna, Austria. <sup>7</sup>Developmental Lung Biology and Cardiovascular Pulmonary Research Laboratories, University of Colorado, Aurora, Colorado, United States.

\*SC and HTP are co-first authors. VJP and GK are co-senior authors.

Running Title: **Adventitial fibroblasts control PASMC phenotype**

Correspondence to:

Grazyna Kwapiszewska

Medical University of Graz

Institute for Lung Health

Neue Stiftungtalstrasse 6/VI, 8010 Graz, Austria

Aulweg 130, Giessen, Germany

E-mail: grazyna.kwapiszewska-marsh@medunigraz.at

## Summary

Pulmonary vascular remodeling is a progressive pathological process characterized by functional alterations within pulmonary artery smooth muscle cells (PASMC) and adventitial fibroblasts (PAAF). Mechanisms driving the transition to a diseased phenotype remain elusive. Utilizing a combination of transcriptomic and proteomic profiling, along with phenotyping of source-matched cells from healthy controls and individuals with idiopathic pulmonary arterial hypertension (IPAH), our investigation uncovered that while PASMC and PAAF retained their original cellular identities, they acquired distinct disease-associated states. Though both cell types exhibited reduced mitochondrial content and hyperpolarization, IPAH-PASMC displayed heightened glycosaminoglycan production and downregulation of contractile machinery, contrasting a hyperproliferative phenotype of IPAH-PAAF. We investigated the involvement of cellular crosstalk in regulating cell state dynamics and identified pentraxin-3 and hepatocyte growth factor as potential modulators of PASMC phenotypic transition orchestrated by PAAF. Our findings contribute to a deeper understanding of pulmonary vascular mesenchyme dynamics in disease pathogenesis.

Keywords: vascular smooth muscle cells, adventitial fibroblasts, integrative omics, cell state transitions, cellular crosstalk

## Introduction

Classical view of vascular smooth muscle cells as resident cells mediating vasoactive responses and adventitial fibroblasts as structural support cells producing fibrillar collagen has been appended by single cell transcriptomics studies in humans. Single cell resolution has helped to define the tissue specific heterogeneity within and delineate the distinctions of vascular resident cell populations to other smooth muscle and fibroblast populations (Crnkovic et al., 2022; Muhl et al., 2022, 2020; Travaglini et al., 2020). Additional layer of cellular complexity and heterogeneity is acquired through the disease process. Fate mapping studies in animal models of systemic and pulmonary vascular disease have shown that the majority of vascular smooth muscle cells and adventitial fibroblasts retain their lineage identity during vascular remodeling (Biasin et al., 2020; Bordenave et al., 2020; Sheikh et al., 2015; Steffes et al., 2020; Wirka et al., 2019; Worssam et al., 2023). However, a subset of these cells exhibits the acquisition or loss of specific markers, such as smooth muscle actin (Chu et al., 2024; Shankman et al., 2015; Short et al., 2004). Nevertheless, diseased cells consistently demonstrate altered expression profiles compared to their healthy counterparts (Crnkovic et al., 2022; Wirka et al., 2019; Worssam et al., 2023; Zhang et al., 2024).

Pulmonary vascular disease is an umbrella term encompassing functional and morphological alterations in lung vasculature, either as a standalone condition or, more often, accompanying chronic lung and heart disease (Humbert et al., 2019). We have previously shown that pulmonary vascular disease and remodeling of pulmonary artery compartment is associated with a skewed cellular communication centered on smooth muscle cells and adventitial fibroblasts (Crnkovic et al., 2022). Moreover, molecular alterations identified *in situ* and freshly isolated cells are at least partially preserved and propagated *in vitro*. For example, pulmonary artery smooth muscle cells (PASMC) and pulmonary artery adventitial fibroblasts (PAAF) isolated from remodeled pulmonary arteries display metabolic and proinflammatory reprogramming that was linked with the progression of pulmonary vascular remodeling (Hong et al., 2017; Li et al., 2023; Sutendra et al., 2010). On transcriptional and proteomic level, PASMC display characteristics of phenotypic shift, namely downregulated expression of contractile machinery and upregulation of extracellular matrix components (Crnkovic et al., 2022; Régent et al., 2016). PAAF were shown to direct the behavior of immune cells and serving as a homing place for the immune cells during vascular remodeling (Chelladurai et al., 2022; El Kasmi et al., 2014; Plecitá-Hlavatá et al., 2023). Cumulatively, results imply a cell-type specific communication network that is perturbed

in the vascular remodeling. It is however unclear to which extent are the changes in expression profiles ultimately mirrored phenotypically.

In the current study, we investigated early passage PASMC and PAAF sourced from the same pulmonary artery of healthy, downsized lung donors or patients with idiopathic form of pulmonary arterial hypertension (IPAH). We have combined integrative omics and network-based analysis with targeted phenotypic screens to identify common and cell-type specific differences. Our aim was to uncover significant phenotypic differences upon pulmonary vascular remodeling and identify a set of key molecular correlates that could serve as surrogate marker defining healthy and diseased cell states in a cell-type specific manner. Our results provide insight into bidirectional cell communication between PASMC and PAAF and the critical role of heterotypic cell-to-cell interaction in cell state maintenance and transition in pulmonary artery compartment.

## Results

### *Distinct omics profiles underlie specialized homeostatic functions of normal PASMC and PAAF*

The overarching aim of the current study was to characterize PASMC and PAAF functionality beyond their classical contractile and structural roles. At first, we focused on defining the normal, healthy cell states by using very early passage (p1) PASMC and PAAF isolated from same (source-matched) pulmonary arteries (PA) of healthy, downsized donors (n=4). We performed deep molecular characterization of RNA and protein expression profiles (Figure 1A, Data S1, S2). Principle component analysis confirmed that molecular distinction between two cell types was preserved in early passage on both transcriptomic and proteomic level (Figure 1B). It also revealed higher interpersonal heterogeneity within PASMC samples, while source-matched PAAF represented as a more homogenous group (Figure 1B). We identified a set of significantly enriched genes/proteins in PASMC (Regulator of G Protein Signaling 5 - RGS5, Insulin Like Growth Factor Binding Protein 5 - IGFBP5, Integrin Alpha 2 – ITGA2, Cysteine and Glycine Rich Protein 1 – CSRP1, Actin Filament Associated Protein 1 – AFAP1) and PAAF (Alcohol Dehydrogenase 1C - ADH1C, Scavenger Receptor Class A Member 5 - SCARA5, Complement Factor D – CFD, Microsomal Glutathione S-Transferase 1 – MGST1, Thioredoxin Related Transmembrane Protein 2 – TMX2) for orthogonal validation (Figure 1C). Some of the molecules were previously associated predominantly with SMC, such as RGS5 and CSRP1 (Crnkovic et al., 2022; Snider et al., 2008), or adventitial fibroblast, such as SCARA5, CFD and MGST1 (Crnkovic et al., 2022; Sikkema et al., 2023) expression. We mapped the location of selected enriched targets by multicolor staining of human lung tissue (Figure 1D, E: n=5). In the pulmonary artery compartment, RGS5 and IGFBP5 positivity overlapped predominantly with ACTA2 (alpha smooth muscle actin) stain, while ADH1C, SCARA5 and CFD were observed mostly in adventitial region marked by PDGFRA (Platelet-Derived Growth Factor Receptor Alpha) (Figure 1D, E). Antibodies used to detect other targets (ITGA2, AFAP1, MGST1, TMX2) yielded inconclusive results due to lack or very weak signal in PASMC/PAAF, with exception of CSRP1. AFAP1 and ITGA2 stained endothelial layer, CSRP1 had medial staining pattern in addition to inflammatory cells, while MGST1 and TMX2 stained mostly inflammatory or epithelial cells (Figure S1A). Comparative analysis of transcriptomic and proteomic data sets revealed a strong, but not complete level of linear correlation between the gene and protein expression profiles (Figure S1B, C). We therefore decided to use an integrated dataset and analyzed all significantly enriched genes

and proteins ( $-\log_{10}(P) > 1.3$ ) between both cell types to achieve stronger and more robust analysis (Figure 1F). A gene set enrichment analysis (GSEA) on gene ontology (GO) terms for biological processes was used to infer functional implications of observed expression profiles. The analysis confirmed polarized and distinct cell-type functional associations, revealing vascular development and cell migration processes for PASMC, and endoplasmatic reticulum protein targeting for PAAF. Additionally, PASMC were associated with processes linked to sterol transport, O-glycosylation, and nerve growth factor signaling (Figure 1F). PAAF on the other hand showed enrichment in mitochondrial metabolic processes and heavy metal ion detoxification (Figure 1F). Applying an additional cutoff by taking into consideration only strongly expressed genes/proteins, we performed an overrepresentation analysis of GO biological processes (Figure 1G). Among top10 processes, there was a clear separation and functional distinction between PASMC and PAAF, with overlap in angiogenesis and adhesion (Figure 1G). Contrasting the canonical functional roles, it was PASMC, rather than PAAF, that showed enrichment for extracellular matrix (ECM) organization (Figure 1G), while PAAF showed enrichment for heavy metal ion response, lipid homeostasis and cell differentiation (Figure 1G). The enrichment of lipid-associated processes in PAAF prompted us to validate the observed results phenotypically. We performed a fuel usage assay using Seahorse metabolic analyzer ( $n=6$ ). Real-time monitoring of oxygen consumption under basal condition and upon specific metabolic inhibitors revealed that PASMC could equally utilize glucose/pyruvate and long chain fatty acids as a fuel source for oxidative metabolism (Figure 1H, I). In contrast, upon blocking fatty acid utilization in Krebs cycle, PAAF had stronger drop in basal respiration rate while PASMC were less sensitive to this maneuver (Figure 1I). PAAF displayed additional significant metabolic differences to PASMC (Figure S2). PAAF had lower oxygen consumption and extracellular acidification rates (Figure S2). Ratio of oxygen consumption to extracellular acidification (OCR/ECAR) revealed that PAAF have relative preference for oxidative phosphorylation compared to PASMC (Figure S2), in line with observed enrichment for mitochondrial respiration processes (Figure 1F). This was further supported by lower glycolytic capacity (Figure S2) and lower mitochondrial proton leak (Figure S2). Cumulatively, molecular and phenotypic profiling revealed specialized homeostatic roles of normal, healthy PASMC and PAAF.

*Preservation of major PASMC- and PAAF- defining features and acquisition of novel IPAH cell states*

We next set out to delineate expression changes defining the diseased, remodeling state. Omics profiling was performed on source-matched PASMC and PAAF isolated from patients with end stage idiopathic

pulmonary arterial hypertension (IPAH, n=4) in comparison to donor samples (Figure 1A). PCA analysis of transcriptomic and proteomic profiles revealed a clear sample separation based on cell type (Figure 2A). However, sample separation based on disease state was less obvious (Figure 2A). We used the supervised multivariate Orthogonal Partial Least Squares Discriminant Analysis (OPLS-DA) method to determine the significance of cell-type and disease-state as parameters that drive sample separation. In the first model iteration, we considered either cell type or disease state as input parameter. OPLS-DA modeling found significant differences in the global transcriptomics and proteomics profiles based only on the cell type, but not disease state (Figure 2B), validating PCA analysis observations. For the second model iteration, we took both cell type and disease state simultaneously as input parameters. In this OPLS-DA model, only in the case of transcriptomic dataset there was significant separation between all four groups (Figure 2C). These results imply that remodeling process results in substantial transcriptional changes (cell state), but that each cell type retains their original cell lineage designation, in line with results from fate mapping and fresh cell single cell transcriptomics (Biasin et al., 2020; Crnkovic et al., 2022, 2018). We accordingly evaluated the preservation of the expression profile and localization in IPAH of donor PASMC- and PAAF-enriched targets. Multicolor staining of IPAH lungs revealed the preserved staining patterns in the pulmonary artery compartment compared to donors, with RGS5 signal associating with ACTA2, while ADH1C, SCARA5 and CFD signals associated with PDGFRA (Figure 2D, Figure S3). IGFBP5 in situ hybridization signal was detected both in PASMC and PAAF regions (Figure 2D). Comparable patterns of target expression were further corroborated by single-cell transcriptomics data from fresh human pulmonary arteries (Crnkovic et al., 2022) with the notable exception of IGFBP5, which was predominantly expressed in PAAF (Figure 2E).

#### *IPAH-defining cell states of PASMC and PAAF in vitro*

We next focused on characterizing disease state-defining features. Gene ontology analysis of selected gene sets from combined transcriptomic and proteomic data (significantly regulated genes/proteins), showed a cell-type specific footprint of molecular changes upon IPAH (Figure 3A). IPAH-PASMC were characterized by upregulation of nucleotide-sugar and lipid biosynthesis, Golgi vesicle transport and endoplasmic reticulum (ER) stress processes, while simultaneously displaying downregulation of cytoskeletal components, ribonucleoprotein complex export and p53 signaling (Figure 3A). IPAH-PAAF upregulated genes and proteins involved in cell proliferation, DNA repair and downregulated expression of NF- $\kappa$ B pathway components, NK-cell activation and transcriptional stress response (Figure 3A). Enrichment for activated sugars and Golgi

transport process is associated with increased synthesis and secretion of glycosylated proteins, such as ECM components. We therefore measured production of proteoglycans on isolated PA using 1,9-dimethylmethylene blue assay. Quantitative analysis revealed increased GAG-content in IPAH (n=8) compared to donor (n=7) PA (Figure 3B). We localized the site of the increased GAG content in PA using Alcian blue staining of human lung tissue. This showed enhanced medial staining in IPAH (n=10) compared to donor (n=10) and prominent signal in neointimal PA compartment (Figure 3C) that was confirmed by quantitative image analysis (Figure 3D). In line with observed enrichment for DNA replication and cell cycle phase regulation (Figure 3A), IPAH-PAAF displayed higher proliferative capacity compared to donor-PAAF, upon both stimulated and unstimulated conditions (Figure 3E). IPAH-PASMC in contrary showed lower proliferative rate compared to donor-PASMC (Figure 3E), corresponding to our previous observation of G1 cell cycle accumulation of IPAH-PASMC (Crnkovic et al., 2022). The observed phenotypic effect is strongest in very early passage and is progressively lost with passaging (Figure 3F). In vitro results mirror indirect determination of cellular proliferation rates *in situ* using PCNA staining of human lung tissue. We observed frequent PCNA+ fibroblasts, identified by PDGFRA staining, in the adventitial layer of PA from IPAH patients (Figure 3G), while decreased percentage of proliferating PASMC in IPAH PA, detected by PCNA and Ki-67 staining, was reported previously (Crnkovic et al., 2022). The attenuated differences in proliferation rates between IPAH and donor cells with prolonged passaging suggest culture-induced cell state changes and a loss of disease-specific phenotypic features. To investigate the stability of key phenotypic differences between IPAH and healthy cells, we analyzed transcriptional signatures in freshly isolated, early-passage, and late-passage cells using published datasets (Chelladurai et al., 2022; Crnkovic et al., 2022; Gorr et al., 2020). Gene set enrichment analysis revealed significant distinctions between fresh and cultured cells, with marked differences in the top-enriched biological processes across all conditions (Data S3). By focusing on the key phenotypic features identified in this study (Figure 3A), we found that IPAH PASMCs exhibit a more gradual phenotypic shift with passaging, in contrast to the sharp changes observed early on in cultured PAAFs (Figure 3H). Early-passage IPAH PASMC (p1) retain positive enrichment for biosynthetic and ECM processes and share positive enrichment for macrophage regulation processes with fresh cells, while simultaneously displaying gradual negative enrichment of contraction associated processes (Figure 3H). Surprisingly, both early (p1)-and late-passage (p6) IPAH PAAF display prominent positive enrichment for cell cycle and proliferation processes, with fresh cells showing weak enrichment for DNA recombination process

(Figure 3H). Even more striking are prominent inverse enrichments for inflammatory/NF- $\kappa$ B signaling between fresh and cultured IPAH PAAF (Figure 3H). Similar, but less pronounced trend for inverse enrichment is displayed for processes involving cellular adhesion and ECM organization (Figure 3H). In summary, expression profile of early passage cells retains some of the key phenotypic features displayed by cells in their native environment.

#### *Shared IPAH expression disturbances in PASMC and PAAF converge on mitochondrial dysfunction*

Distinct remodeling expression profiles and cell behavior, led us to search if there are any common molecular perturbations shared between IPAH-PASMC and IPAH-PAAF. Number of co-directionally regulated genes and proteins were limited to 47 (Figure 4A). Further selection based on significance and fold change provided a list of most significantly regulated molecules in IPAH that are shared between PASMC and PAAF (Figure 4B, highlighted corners bottom left and top right). Using this as an input for network analysis based on the STRING database, we built the underlying gene interaction network and identify shared upstream regulating factors (Figure 4C). Only a fraction of commonly regulated genes and proteins were encompassed by the putative regulatory network (Figure 4C). For the remaining molecules, it was not possible to construct an interaction map, implying regulation by independent mechanisms and upstream regulators. We therefore focused further on those molecules that were encompassed in the interaction network. Interestingly, their regulatory nodes converged on the immuno-inflammatory and survival-apoptosis regulators and effectors (Figure 4C). Specifically, a majority of the nodes building the interaction network belonged to a limited set of genes comprising mostly cytokines/chemokines (IL1B, IL2, IL4, IL6, IL10, TNF, CCL2, CXCL8) and inflammatory-stress response signal transduction pathways (JNK, AKT, NF- $\kappa$ B, STAT3, MYC, JUN) (Figure 4C). Additional pathway enrichment analysis based on the BioPlanet database, uncovered regulation of apoptosis as a shared pathway by both cell types in IPAH (Figure 4D). Shared SOD2 (mitochondrial superoxide dismutase 2) downregulation prompted us to investigate the mitochondrial function and redox defenses. We performed tetramethylrhodamine methyl ester (TMRM) staining for the detection of mitochondrial content and potential. Cellular mitochondrial content was lower both in IPAH-PASMC and IPAH-PAAF upon removal of serum and growth factors (starvation) (Figure 4E). However, the remaining mitochondria in IPAH cells were hyperpolarized (Figure 4F). Mitochondrial membrane hyperpolarization is linked with increased reactive oxygen species (ROS) production. We measured cellular ROS production using CellRox Deep Red dye at basal levels and upon PDGF-BB stimulation revealing that only IPAH-PASMC

significantly upregulate ROS production (Figure 4G). Although mitochondrial dysfunction seems as a common underlying disturbance between cell types in IPAH, the downstream consequences appear to be cell-type selective. Mitochondrial dysfunction and elevated ROS production are associated with increased apoptosis, aligning with reduced SOD2, which plays a role in clearing mitochondrial ROS and mitigating oxidative stress to protect against cell death. (Kokoszka et al., 2001) (Figure 4D). We therefore assessed *in situ* the rate of apoptosis using terminal deoxynucleotidyl transferase dUTP nick end labeling (TUNEL) assay on human lung tissue samples from donors and IPAH patients (n=6 for each condition) and co-stained with ACTA2 and PDGFRA (Figure 4H). However, apoptosis measured as TUNEL+ cells was in both cases a very rare event (1-2 positive ACTA2 or PDGFRA PA cells per slide) that no meaningful quantification was possible.

#### *PASMC and PAAF acquire divergent disease-cell states*

Contrasting the limited overlap in regulated elements between PASMC and PAAF, vast majority of IPAH transcriptomic and proteomic changes (more than a thousand genes/proteins) were uniquely regulated between the cell types, including substantial number of inversely regulated molecules (Figure 5A). PASMC possessed more pronounced changes than PAAF as shown by the number of differentially regulated genes and proteins in IPAH (Figure 5B). A STRING based interaction network, overlaid with information about the initial cell-type association under normal condition (preferential enrichment in donor PASMC or PAAF) (Figure 5B), revealed that the majority of down-regulated molecules in IPAH-PASMC came from a set of genes and proteins preferentially expressed by PASMC in healthy state (donor-PASMC) (Figure 5B). This reflects the fact that most downregulation in PASMC takes place in contractile machinery elements (Figure 3A) that are characteristic for smooth muscle cell lineage. In contrast, molecules upregulated in IPAH-PASMC contained targets from both PASMC and PAAF enriched data set under healthy cell states (donors). IPAH-regulated molecules in PAAF on the other hand could be traced back to both PASMC- and PAAF-enriched normal cell state (Figure 5B). Gene ontology analysis of IPAH revealed a clear cell-type distinct fingerprint of molecular changes: PASMC harbored expression changes in biological processes related to ECM, while cell cycle and replication processes were enriched in PAAF (Figure 5C). Looking selectively at top20 differentially regulated genes, a similar pattern was observed: genes that were down-regulated in IPAH-PASMC, such as SHROOM3, BLID or CCK, were preferentially expressed by donor PASMC, while upregulated genes such as chemokines (CCL7, CCL26) were not restricted to smooth muscles (Figure 5D). For comparison, expression of the same genes in PAAF was not significant (Figure 5D). The same was observed for top20

differentially regulated genes in IPAH PAAF – their expression was not significantly changed in PASMC (Figure 5E). However, osteoprotegerin (TNFRSF11B) and matrix metalloproteinase 1 (MMP1), genes with most pronounced expression change in IPAH PAAF, are enriched in PASMC (Figure 5E). These examples show the importance of distinguishing cell-type specific contributions to gene/protein expression levels. It also implies cell-type specific regulatory mechanisms at play.

Biological function assignment of top20 regulated elements in PASMC and PAAF entailed a broad spectrum of assigned biological functions, ranging from motility, adhesion, hydrolysis, metabolism, growth, differentiation, and ECM components. We wondered if a gene/protein-level evaluation of significantly changed elements for each cell type between IPAH and donors, could give indication of putative phenotypic changes in addition to pathway enrichment approach. We manually curated significantly changed elements in IPAH PASMC (Figure 5F, outermost circle) and IPAH PAAF (Figure 5F, middle circle) and grouped them in ECM, immune system, metabolism, and cell cycle categories (Figure 5F). Elements that additionally had significantly differing regulations between PASMC and PAAF under IPAH conditions were marked bold (Figure 5F, black bordering and bold font). We also provide reference if a particular element was preferentially expressed in PASMC or PAAF (Figure 5F, innermost circle). Striking feature is that both cell types display perturbations in all four major functional categories, the involved genes/proteins are different. For instance, IPAH PASMC upregulate proinflammatory cytokines (CCL7, CCL26) and ECM components claudin 14 (CLDN14) and metalloproteinase ADAMTS18, while IPAH PAAF downregulate anti-inflammatory NF- $\kappa$ B component RelB and laminin 1 (LAMA1) and matrix metallopeptidase 1 (MMP1) ECM components (Figure 5F). Generally, PASMC and PAAF take a divergent path upon vascular remodeling: while IPAH-PASMC acquire synthetic phenotype with up regulation of chemotactic elements, IPAH-PAAF display hallmarks of fast-cycling cells. Based on these results, we wondered if ECM-based phenotypic assays could uncover cell type and state distinct responses, similarly to results obtained by proliferation and metabolic assays.

#### *ECM components centered signaling elicits cell type and cell state distinct phenotypic responses*

Changes in ECM composition are a recurring hallmark of pulmonary vascular remodeling (Hoffmann et al., 2015, 2014; Jandl et al., 2020; Mutgan et al., 2024) recapitulated also in current omics dataset (Figure 5F). Ligand-receptor interaction analysis of our omics dataset indicated that ligand expressing PAAF might act as sender cell type and PASMC as receiver cells through their integrin receptor repertoire expression (Figure 6A). ITGA2 and ITGB1 subunits expressed in PASMC build a heterodimer complex functioning both as

laminin and collagen receptor (Languino et al., 1989) (Figure 6B). We speculated that change in laminin-to-collagen ratio in ECM would have functional consequence and influence phenotypic behavior of cells in contact with altered ECM. We measured attachment and motility properties of cells with respect to these two substrates. Both PASMC and PAAF (n=6) displayed striking phenotypic differences depending on surface coating. Whereas cells on collagen-coated surface had spread-out shape with several protrusions (Figure 6C), laminin coating inhibited cell spreading and cells obtained a more symmetric, round-like appearance (Figure 6C). PASMC, both donor and IPA, attached less efficiently to laminin compared to collagen-coated surfaces (Figure 6D), but only donor-PAAF displayed comparable behavior (Figure 6D). Although not significant, IPA-PASMC had tendentially higher attachment on laminin-coated surface compared to donor-PASMC (Figure 6D). This trend was again observed in an additional assay measuring gap closure on collagen- or laminin-coated surface (Figure 6E, n=2-6). At early time points, donor PASMC showed widening gap area before final gap closure on laminin coating (Figure 6E). On collagen coating, potential difference was observed at later time point and showed a reverse trend (Figure 6E), probably due to influence of higher proliferative rate of donor PASMC compared to IPA PASMC (Figure 3E), rather than acute effects of attachment and migration that have more influence in early time points. On both substrates, PAAF revealed a faster gap closure compared to PASMC (Figure 6E), likely in line with their higher proliferative capacity (Figure 3E). The expression profile of integrin subunits serving as high-affinity collagen ( $\alpha 2\beta 1$ ) or laminin receptors ( $\alpha 3\beta 1$ ,  $\alpha 6\beta 1$ ) (Moiseeva, 2001) was higher in cultured PASMC compared to PAAF, with minimal change in the disease state (Figure 6F). A similar profile was detected in fresh cell, whereby IPA PAAF displayed increased expression of alpha2 and alpha6 subunits (Figure 6G).

In addition to changes in collagen and laminin class of ECM components, expression profile of proteoglycans showed both cell type and cell state distinct pattern with IPA-PASMC characterized by significant enrichment in this ECM family (Figure 3B-D). Among other functions, proteoglycans serve as regulators of the complement system (Clark et al., 2013). PAAF display enrichment for complement components such as CFD (Figure 1E) and IPA-PAAF were identified to drive inflammation through classical complement pathway (Frid et al., 2020). Two biologically active cleavage products, C3a and C5a, are released in this process and both PASMC and PAAF express corresponding receptors (Figure S4). We therefore tested a possible feedback loop between the activated complement system and enhanced proteoglycan expression in IPA. We stimulated donor and IPA cells with C3a and C5a and measured expression levels of versican

(VCAN, PASMC enriched) and decorin (DCN, PAAF enriched) proteoglycans (Crnkovic et al., 2022). Both VCAN (n=4) and DCN (n=6) showed a trend or had significantly higher expression level in IPAH cells (Figure 6H, I). However, only donor PAAF responded to C3a and C5a stimulation and displayed IPAH-state-like expression levels of DCN (Figure 6I). In summary, these results provide a differential phenotypic readout and link the observed ECM expression changes in a cell type and cell state specific manner, with PAAF serving generally as sender type and PASMC as responders, excluding the PAAF autocrine complement response.

#### *IPAH-PAAF modulate phenotypic hallmarks of PASMC*

In order to analyze PASMC-PAAF communication in a more comprehensive manner, we took advantage of our published single cell RNA sequencing dataset from human PA (Crnkovic et al., 2022). We extracted PAAF and PASMC clusters and performed intercellular communication network analysis using CellChat. This revealed a skewed PAAF-to-PASMC signaling in IPAH state towards secreted ligands (Figure 7A, Figure S5, S6). We also performed alternative cell-cell interaction analysis using NicheNet and filtered resulting ligand-receptor pairs for secreted signaling using CellChat database annotation. Merged CellChat and NicheNet analysis results revealed a set of functionally-relevant soluble ligands such as IL1A, POSTN, PDGFA/B, FGF2, BMP2/4, CD40LG perturbed in IPAH state (Figure 7B). We therefore asked if cellular crosstalk is able to modulate phenotypic markers using a co-culture model. As reference, we used source-matched donor-PASMC and PAAF (n=3) that were directly co-cultured for 24 hours followed by sorting and quantitative PCR analysis (Figure 7C). Expression levels of selected cell-type and cell state markers were determined as a readout of phenotypic modulation. Simultaneously, same donor cells were co-cultured with IPAH cells from the other cell type, producing a combinatorial readout to assess PASMC-to-PAAF and PAAF-to-PASMC crosstalk (Figure 7C). Results revealed that co-culture of donor-PASMC with IPAH-PAAF (n=3) lead to partial loss of healthy state PASMC markers (CNN1, RHOA) without affecting the expression of disease-state markers (VCAN, BGN) (Figure 7D). Expression of neither healthy nor disease state PAAF markers was affected in donor-PAAF co-cultured with IPAH-PASMC (n=3) (Figure 7D). To get a better understanding on donor-PASMC state shift induced by co-culture with IPAH-PAAF, we performed bulk RNA-Seq on collected samples. As the effect of 24h co-culture was mild compared to sample-driven variability, we performed model correction to account for paired PASMC samples in our experimental setup. The resulting gene set enrichment analysis on significantly regulated genes (Data S4) showed that genes upregulated in PASMC

by IPAH-PAAF co-culture mediate inflammatory processes and signaling, apoptosis and proliferation (Figure 7E).

We next went on to identify possible PAAF ligands that could drive the observed phenotypic change in PASMC. As our proteomics approach sampled only proteins from the cell lysate, we additionally performed protein array-based screening of 137 unique soluble factors secreted from donor- compared to IPAH-PAAF (n=4) (Figure 7F, Figure S7A). We selected for factors whose expression levels were changed 10% or more in at least two samples and performed clustering of tested samples and factors providing a list of 44 potential regulators (Figure 7G). As some of those factors were already known and investigated in the context of IPAH, we focused on finding potentially novel PAAF-derived regulators of SMC phenotype. In order to narrow down the search, we used hierarchical clustering to group co-regulated ligands into smaller number of groups. Similarity matrix revealed one major and six minor clusters of factors showing correlated changes among 4 comparison pairs (Figure S7B). One cluster was characterized by co-regulated chitinase 3-like 1, insulin-like growth factor-binding protein 3 (IGFBP-3) and angiogenin expression pattern; other clusters with Extracellular Matrix Metalloproteinase Inducer (EMMPRIN), Epithelial-Derived Neutrophil-Activating Protein 78 (ENA-78), and Vascular Endothelial Growth Factor A (VEGF) secretion, respectively (Figure S7). Three additional clusters involved upregulated secretion of Epidermal Growth Factor (EGF), hepatocyte growth factor (HGF), and chemerin with correlated pentraxin-3 (PTX3) downregulation (Figure S7). Based on further literature search, we excluded ligands with reported link to PAH and selected chitinase 3-like 1, IGFBP-3, angiogenin, HGF, and PTX3 for further validation. Stimulation of donor and IPAH PASMC (n=6) with HGF and PTX3 displayed the most consistent effects on modulation of PASMC cell state markers (Figure 7H), while other tested ligands mostly lacked the effect on donor PASMC and were not investigated further (Figure S8). Intriguingly, HGF and PTX3 seem to have opposite effect on vascular smooth muscle cells, with PTX3 inhibiting neointima formation (Camozzi et al., 2005) and HGF promoting pulmonary vascular remodeling (Park et al., 2022). Indeed, stimulation of PASMC with PTX3 preserved the expression of contractile markers in donor cells, but not in IPAH, while HGF downregulated contractile state markers in donor IPAH and increased disease state marker VCAN in IPAH PASMC (Figure 7H).

## Discussion

Effective treatment of pulmonary arterial remodeling has been elusive over the years (Stacher et al., 2012). IPAH is characterized by recalcitrant morphological changes and persistent alterations in cellular function. Studies have indicated that PASMC and PAAF retain these disease-associated changes in *in vitro* conditions (Stenmark et al., 2018; Viswanathan et al., 2023; Zhang et al., 2017). Our current results using transcriptomic and proteomic profiling in combination with phenotypic screening demonstrate that PASMC and PAAF acquire distinct IPAH-associated cell states, while retaining their original cell type designation. This shift from healthy to diseased state is a cell type-specific process and results with functionally meaningful differences between cell types. Furthermore, we identify that maintenance of PASMC cell state is dependent on external cues, such as ECM components and soluble ligands, provided in part by neighboring PAAF. The divergent fates and distinct disease states that cells acquire, can be traced to initial cell lineage differences that are formed and imprinted in a tissue- and anatomical location-specific manner (Muhl et al., 2022, 2020). These anatomical-location based distinctions provide fibroblast and smooth muscle cell lineages with phenotypic potential beyond canonically assigned roles.

Expression of three selected markers in PAAF, scavenger receptor class A member 5 (SCARA5), complement factor D (CFD) and alcohol dehydrogenase 1C (ADH1C), provide the best example of PAAF pleiotropic roles beyond mere ECM production and structural support. PAAF, being at the outer barrier of vessels, might act as innate immunity sentinels with adventitia being the main compartment of inflammatory reaction and homing site for inflammatory cells (Dahlgren et al., 2019). CFD activates the alternative pathway of the complement triggering chemotaxis and inflammation (White et al., 1992). SCARA5, a ferritin scavenger receptor that mediates cellular iron uptake, limits the extracellular iron concentration (Li et al., 2009). Going beyond putative immunomodulatory functions, we additionally reveal PAAF involvement in lipid metabolism at expression profile and phenotypic level. This functionality perhaps reflects broader ontogenetic potential of PDGFRA+ cells as adipocyte precursors (Angueira et al., 2021): PAAF express ADH1C, enzyme involved in metabolism of lipid peroxidation products and hydroxysteroids (Höög and Ostberg, 2011), PPARG, a key transcriptional regulator of lipid metabolism, and APOE, a lipid handling protein (Table S1, S2). All three homeostatic functions, complement regulation, iron handling and lipid metabolism, seem to be co-opted and distorted in PAH pathomechanism (Frid et al., 2020; Ruiter et al., 2011; Zhang et al., 2017).

Simultaneously, acquisition of disease cell state by the PASMC follows a different course. Firstly, we observed that already healthy PASMC display intrinsically higher heterogeneity compared to PAAF. Enrichment in developmental, morphogenesis, migration, and signal transduction biological processes coupled with higher metabolic rate, both oxidative and glycolytic, provides PASMC with functional flexibility and adaptability in response to various injuries. Expression of regulator of G protein signaling 5 (RGS5) provides an example of the plasticity potential imprinted in normal PASMC. RGS5, for instance, as a gatekeeper of G protein signaling and signal transduction modulator, influences and fine-tunes the PASMC response to external cue (Wang et al., 2008). Under normal condition, expression of contractile machinery coupled with higher metabolic rate, enables PASMC to fulfill their homeostatic role in providing vasoactive function and structural support for endothelial lined lumen. However, one of the defining vascular SMC characteristic and adaptation to vascular insult, including that of IPAH-PASMC cell state, is downregulated expression of the cytoskeletal contractile elements. This seems to be an intrinsic, “programmed” response of SMC to remodeling, rather than vasodilator therapy-induced selection pressure. Similar phenotypic change is observed in SMC from systemic circulation (Gomez and Owens, 2012) and animal model of pulmonary hypertension without exposure to PAH medication (Crnkovic et al., 2023). We suspect that isolated decrease in contractile machinery would dampen both the contraction and relaxation properties of the PASMC, affecting not only its response to dilating agents, but also to vasoconstrictors. Clinical consequences and responsiveness to dilating agents are more difficult to predict, since the vasoactive response would additionally depend on mechanical properties of the pulmonary artery defined by cellular and ECM composition (Thenappan et al., 2018).

Distinctive cell type characteristics of PASMC and PAAF come into play during disease process of pulmonary vascular remodeling, testified by low overlap in commonly perturbed pathways and associated genes/proteins between PASMC and PAAF in IPAH. PAAF and PASMC acquire distinct cell states upon remodeling with IPAH-PAAF showing enrichment in DNA replication and repair processes and accompanying hyperproliferative phenotype. IPAH-PASMC in addition to partial loss of contractile markers alter their metabolic profile to support the increased biosynthetic demand. In line with this notion, we have observed significant downregulation of enolase 3, malate dehydrogenase 1B, pyruvate dehydrogenase kinases, and phosphofructokinase, and up-regulation of glutamine-fructose-6-phosphate transaminase 2 in IPAH-PASMC (Supplemental Table 1, 2). This profile indicated potential glucose shunting into hexosamine pathway (Barnes

et al., 2015; Buse, 2006). Hexosamine biosynthetic pathway is a side branch of glycolysis utilized for generation of amino-sugars and subsequent protein and lipid glycosylation, including glycosaminoglycans and PG synthesis (Buse, 2006). The mostly enriched ECM class next to classical fibrillar collagens, were PG, in line with previously published reports (Barnes et al., 2015; Chang et al., 2016; Crnkovic et al., 2022; Jandl et al., 2020; Mutgan et al., 2024). Due to the complex structure of PG, they can withstand high pressure, modulate cellular phenotype and thus be a necessary part of the adaptation or maladaptation process (Wight and Merrilees, 2004).

Despite broad changes in expression profiles in both cell types upon vascular remodeling and strikingly low overlap in perturbed pathways between PASMC and PAAF, they nevertheless share one common feature. Expression pattern of key cell type-enriched elements is preserved in the diseased state. This finding is further supported by the global analysis of transcriptomic and proteomic profiles revealing that cell type as a variable has a stronger influence on sample distinction than disease condition. In other words, majority of IPAH PASMC are still more alike to donor PASMC than to any PAAF.

Interestingly both cell types share a common disturbance in mitochondria characterized by lower IPAH mitochondrial content and hyperpolarized mitochondrial membrane potential. Nevertheless, ultimate phenotypic consequences of such a change still seems to be divergent for each cell type, as implied by distinct stimulated ROS response. Whether mitochondrial disturbance is one the initial cause of the disease or its consequence, as a common point it offers a potential action point to revert cell states from different lineages towards a normal, homeostatic condition, in line with reports on restoring SOD2 expression as a viable therapeutic target (Paulin et al., 2014; Plecitá-Hlavatá et al., 2023).

Going beyond cataloguing molecular and functional changes, we address the underlying communication mechanisms responsible for maintenance and transition between identified cell states. We first dissect the role of ECM composition and reveal how a relative change in the laminin-to-collagen ratio, driven by a shift in PAAF cell state, similarly alters the spreading, attachment, migration, and expansion of both normal and diseased PASMCs. The comparable responses of donor and IPAH PASMC likely result from their shared integrin receptor expression profiles. Meanwhile, ECM class switching engages different high-affinity integrin receptors, which activate alternative downstream signaling pathways (Nguyen et al., 2000) and lead to differential responses to collagen and laminin matrices. We thus propose a model in which laminins and

collagens act as PAAF-secreted ligands, regulating PASMC behavior through their ECM-sensing integrin receptors.

We also uncover an autocrine loop centered on PAAF and showing how activated complement pathway can drive expression of PAAF-enriched ECM components. These processes could induce a more invasive cellular phenotype and potentially promote neointima formation. One could trace this PASMC susceptibility to ECM composition change to their enriched expression in integrin subunits serving as collagen and laminin receptors, making them uniquely primed to sense and respond to external cues. However, the same mechanism renders cells susceptible to phenotypic change induced simply by extended *in vitro* culturing, testified by broad expression profile differences between fresh and cultured cells. This common caveat in cell biology research and represents a technical and practical tradeoff that requires cross validation of key findings. Using a combination of archived lung tissue and available single cell RNA sequencing dataset of human pulmonary arteries, we show that some of the key defining phenotypic features of diseased cells, such as altered proliferation rate and ECM production, are preserved and gradually lost upon prolonged culturing. Interestingly, this culturing effect was more pronounced in PAAF particularly with respect to inverse direction of enrichment for inflammatory/cytokine signaling process. The removal of PAAF from their native immunomodulatory environment and the presence of hydrocortisone in PAAF culture media could provide a potential explanation for this effect.

We extend our investigations more broadly and uncover a general shift in IPAH-PAAF secretome being sufficient to induce significant phenotypic changes in normal PASMC. Among several deregulated ligands, we identify downregulated expression of PTX3, a protective factor, and upregulation of HGF, pathogenic factor, as PAAF-sourced regulators of PASMC cell state. PTX3 counteracts pro-proliferative action of fibroblast growth factor and its overexpression attenuates neointima formation in systemic arteries (Camozzi et al., 2005). Conversely, upregulation of HGF/cMet pathway in endothelial cells upon Sox17 loss was associated with PAH promotion (Park et al., 2022). We would therefore argue that potential exploratory clinical trial for pulmonary vascular disease could entail a combination therapy consisting of recombinant PTX3 and HGF blocking antibody or c-Met inhibitor. However, the identified factors likely represent just a fraction of ligands expressed by other cell types present in the pulmonary artery compartment. The influence of endothelial and inflammatory cells on PASMC and PAAF phenotype requires further investigation.

A low case number and end-stage disease samples used for omics characterization represents a study limitation that has to be taken into account before assuming similar findings would be evident in the entire PAH patient population over the course of the disease development and progression.

Nevertheless, our results provide detailed understanding of functional changes in relation to underlying molecular expression differences upon pulmonary vascular remodeling. Furthermore, we identify novel targets for cell-type specific correction of diseased cell states and potential reverse remodeling strategies.

## Acknowledgments

We appreciate excellent technical assistance from Julia Kohlbacher, Hans Peter Ziegler and Elisabeth Blanz. Schematic figure panels for this article are created with BioRender.com. This work was supported by Cardio-Pulmonary Institute EXC 2026 390649896 (GK) and Austrian Science Fund (FWF) grant I 4651-B (SC). For open access purposes, the author has applied a CC BY public copyright license to any author accepted manuscript version arising from this submission.

## Author contributions

Conceptualization: SC, HTP, VJP, GK

Methodology: HTP, JW, MB, AW, IM, AM, RL, ASO, NB, SLH, NR

Investigation: SC, VB, JW, EB, AW, IM, BMN, ME, MW, NR

Visualization: HTP, SM, FV

Supervision: VJP, GK

Writing—original draft: SC, HTP

Writing—review & editing: KH, AO, KS, LMM, VJP, GK

## Declaration of interests

The authors declare no competing interests.

## Data and materials availability:

Genome-wide expression profiling and RNA-Seq data is deposited to the National Center of Biotechnology Information Gene Expression Omnibus database (accession numbers GSE255669, GSE262069). Human tissue samples can be provided pending ethical approval and completed material transfer agreement.

## Figure Legends

### Figure 1. Omics-assisted phenotypic characterization of cell states in healthy human pulmonary artery smooth muscle (PASMC) and adventitial fibroblast (PAAF) lineages.

A) Schematic representation of the experimental setup using early passage cells (n=4). Created in BioRender. B) 3D score plots of principal component analyses (PCA), larger nodes represent gravity centers. C) Volcano plots of  $\log_2$  fold change between donor PASMC and PAAF plotted against significance (- $\log_{10}(P)$ ). Genes names depicted for the top20 transcriptomics hits and proteins above the threshold (- $\log_{10}(P)>1.3$  | LFC |  $>1$ ). D) Immunofluorescent localization of PASMC (ACTA2, RGS5) and PAAF markers (PDGFRA, ADH1C) in normal human lungs (n=5). E) *In situ* hybridization localization of PASMC (IGFBP5) and PAAF markers (CFD, SCARA5). DAPI as nuclear counterstaining. White bar depicting 50  $\mu\text{m}$  (5  $\mu\text{m}$  for zoomed in panels). F) Gene Set Enrichment Analysis (GSEA) of all significantly regulated transcriptomics and proteomics targets between donor PASMC and PAAF using the gene ontology (GO) database. Parent-to-root node visualization (intermediate terms omitted) with node size reflecting significance. Highlighted nodes depict significantly altered GO overview terms being higher expressed in either PASMC or PAAF. G) Top GO terms resulting from an Overrepresentation Analysis (ORA) of the omics dataset using more stringent cutoff values (- $\log_{10}(P) >3$  | LFC |  $>2$  transcriptomics; - $\log_{10}(P) >1.5$  | LFC |  $>0.5$  proteomics). H) Calculated change in basal oxygen consumption rate upon addition of UK5099 (glucose/pyruvate mitochondrial uptake inhibitor) and I) etomoxir (long chain fatty acid mitochondrial uptake inhibitor). Mann-Whitney test,  $p<0.05$ .

### Figure 2. Preserved lineages and distinct PASMC/PAAF cell states in idiopathic pulmonary arterial hypertension (IPAH).

A) 3D score plots of principal component analyses (PCA), larger nodes represent gravity centers. B) Orthogonal projection to latent structures-discriminant analysis (OPLS-DA) T score plots separating predictive variability (x-axis), attributed to biological grouping, and non-predictive variability (technical/inter-individual, y-axis). Monofactorial OPLS-DA model for separation according to cell type or disease. C) Bifactorial OPLS-DA model considering cell type and disease simultaneously. Ellipse depicting the 95% confidence region, Q2 denoting model's predictive power (significance: Q2>50%) and R2Y representing proportion of variance in the response variable explained by the model (higher values indicating better fit). D) Immunofluorescent and *in situ* hybridization localization of PASMC (ACTA2, RGS5, IGFBP5) and PAAF

markers (PDGFRA, ADH1C, CFD, SCARA5) in IPAH human lungs (n=5). White bar depicting 50  $\mu\text{m}$  (5  $\mu\text{m}$  for zoomed in panels). E) Dot plot showing relative expression of omics-identified PASMC/PAAF markers in published single cell transcriptomics dataset of fresh human pulmonary arteries of donors and IPAH patients (GSE210248).

**Figure 3. Phenotypic correlates of PASMC/PAAF cell state in idiopathic pulmonary arterial hypertension (IPAH).**

A) Top 5 biological process terms from the gene ontology enrichment analysis that are up- or downregulated in IPAH. B) Dimethylmethylene blue (DMMB) assay for quantification of glycosaminoglycan content in isolated pulmonary arteries from donor (n=7) or IPAH (n=8) patients. Mann Whitney test. C) Representative Alcian blue (glycosaminoglycans – blue) with Verhoeff's staining (elastic fibers – black/gray) of donor and IPAH lungs. Scale bar 100  $\mu\text{m}$ . Annotated regions depicting adventitia (white), media (yellow), neointima (red). D) Quantitative image analysis of Alcian blue staining intensities in adventitial, medial and neointimal regions of pulmonary arteries from donors (n=10) and IPAH patients (n=10). 2-way ANOVA followed by Sidak's multiple comparisons test (\*p<0.05). E) Proliferative response of passage 3 cells measured by [<sup>3</sup>H]-thymidine incorporation assay upon serum stimulation. Dots represent mean values (n=5-6 donors/IPAH) with bars showing standard errors of mean. Interaction effects of stimulation, cell type, and disease state on cellular proliferation were analyzed by 3-way ANOVA. Significant interaction effects are indicated as follows: \* for stimulation  $\times$  cell type interactions and # for cell type  $\times$  disease state interactions (both \*, # p<0.05). F) Absolute cell counts measured after 24h growth. Mann-Whitney test, p<0.05. G) Representative immunofluorescent localization of proliferating (PCNA marker) PASMC (ACTA2, yellow arrow) and PAAF (PDGFRA, white arrowhead) in health (donor) and diseased (IPAH) lungs. Immune cells were identified through CD45 expression. DAPI nuclear counterstain, 50  $\mu\text{m}$  scale bar. H) Comparison of gene expression changes in IPAH cells compared to healthy state in three conditions (fresh - GSE210248; passage 1 - GSE255669; and passage 3 - GSE144274 or passage 6 - GSE144932). Dotplot of gene set enrichment analysis for selected biological process terms with dot size depicting absolute value of the normalized enrichment score (absNES), color intensity showing significance level ( $\log_{10}p$ ) and color-coding for up- or downregulation of the biological process.

#### Figure 4. Mitochondrial dysfunction as an intersecting phenotypic characteristic of PASMC and PAAF in IPAH.

A) Euler diagram of the differentially expressed genes summarizing the overlaps and disjoints in regulation (criteria employed:  $-\log_{10}(P) > 1.3$ ; and  $LFC \pm |1|$  for transcriptomics data and  $\pm |0.5|$  for proteomics data). B) Scatter plot graph of  $\log_2$  fold changes between donor and IPAH in PASMC plotted against changes in PAAF, shaded areas highlighting commonly regulated genes/proteins. C) Visualization of STRING-based interaction and regulatory network with gray nodes representing identified putative upstream regulators. D) Pathway analysis performed in Enrichr using the BioPlanet database with a matrix annotating the main genes involved with color coding reflecting the IPAH dependent regulation. E) Mitochondrial content measurement using TMRM dye in complete or starvation (no serum) medium. F) TMRM dye (quench mode) based mitochondrial membrane potential measurement following starvation. G) Basal and PDGF-BB-stimulated reactive oxygen species production (ROS) (40minutes, 50 ng/mL) using CellRox DeepRed dye. Kruskal-Wallis test followed by Dunn's multiple comparisons test. Cell numbers from each condition and cell type denoted by N on the graph (n=3 independent donors/IPAH) (E-G). H) Representative immunofluorescent localization of apoptotic cells (TUNEL marker). PASMC (ACTA2 marker) and PAAF (PDGFRA marker) in health (donor) and diseased (IPAH) lungs (n=6). DAPI nuclear counterstain, 25  $\mu$ m scale bar (5  $\mu$ m for zoomed in panel).

#### Figure 5. Cell type specific IPAH dependent transcriptomic and proteomic changes

A) Dot plot of  $\log_2$  fold changes between donor and IPAH in PASMC plotted against changes in PAAF, shaded areas highlighting the inversely regulated genes/proteins (criteria employed:  $-\log_{10}(P) > 1.3$ ; and  $LFC \pm |1|$  for transcriptomics data and  $\pm |0.5|$  for proteomics data). B) A synoptic view of the network analysis performed with all uniquely regulated elements (as highlighted in A), depicting their initial enrichment in donor cell type. C) Significant terms resulting from a gene ontology enrichment analysis of uniquely regulated elements represented as nodes connecting to related nodes, reflecting which cell type mostly contributed to the changes observed. Color depicting significantly regulated elements in omics dataset. D) Top 20 most significantly regulated genes in IPAH PASMC and E) IPAH PAAF. Color coding reflects the IPAH dependent regulation, and initial enrichment in donor cell type. F) Circular heatmap of IPAH dependent regulation of metabolic, extracellular matrix, immune system and cell cycle elements in PASMC and PAAF. The two outer rings give information of direction and intensity of change in IPAH-PASMC (ring panel III) and IPAH PAAF

(ring panel II), while the inner most ring (ring panel I) depicts initial cell-type enrichment at normal condition. Highlights (bold font) are given to significantly differing regulations between PASMC and PAAF under IPAH conditions. The functional association is performed based on data extracted from GeneCards, following a manual curation.

**Figure 6. IPAH dependent changes mediated through cell type distinct extracellular matrix response.**

A) Ligand-receptor interaction analysis for PAAF and PASMC based on transcriptomic and proteomic data set. B) STRING physical interaction network for PASMC expressed receptors (red, ITGA2 and ITGB1) and PAAF expressed ligands (blue, COL3A1 and LAMA1). Edge thickness indicating strength of data support. C) Representative image of crystal violet-stained attached cells on collagen-I or laminin coated plates. 200  $\mu$ m scale bar. D) Attachment assay for donor and IPAH PASMC and PAAF (n=5-6) on collagen-I and laminin coated plates (n=6 for each condition). 2-way ANOVA followed by Dunnett's multiple comparisons test (\*p<0.05) for each cell type. E) Gap closure assay on collagen-1 (donor/IPAH PASMC n=3/5, donor/IPAH PAAF n=5/6) or laminin-coated (donor/IPAH PASMC n=2/3, donor/IPAH PAAF n=6/6) plates. Mean values (presented as % of gap area) over time with standard error mean. F) Mean gene expression values in p1 cells of integrin subunits functioning as collagen and laminin receptors (GSE255669, Data S1). G) Relative expression of integrin subunits in published single cell transcriptomics dataset of fresh human pulmonary arteries of donors and IPAH patients (GSE210248). H) Versican gene expression in PASMC stimulated 24h with active complement components C3a or C5a (100 ng/mL). I) Decorin gene expression in PAAF stimulated 24h with active complement components C3a or C5a (100 ng/mL). Mann-Whitney test (\*p<0.05).

**Figure 7. Skewed expression profile of PASMC cell-state markers mediated by IPAH-dependent changes in PAAF ligands.**

A) Ligand-receptor interaction analysis for PAAF and PASMC based on single cell RNA sequencing dataset. B) Circos plot showing consensus soluble ligand and cognate receptor pairs identified by CellChat and NicheNet analysis of PAAF or PASMC as sender (ligand-expressing) cell type. C) Schematic representation of PASMC-PAAF co-culture experiment to determine the influence of IPAH cells on phenotypic marker expression in donor cells. Created in BioRender. D) Gene expression of health (calponin: CNN1, Ras Homolog Family Member A: RHOA, peroxisome proliferator-activated receptor gamma: PPARG, osteoprotegerin: TNRSF11B) and disease (versican: VCAN, biglycan: BGN, cyclin D1: CCND1) state

phenotypic markers in donor PASMC (upper row) and donor PAAF (lower row) following their co-culture with IPAH cells. E) Top 10 gene ontology biological processes enriched in the set of significantly upregulated genes in donor-PASMC co-cultured with IPAH-PAAF compared to reference (source-matched donor-PAAF). F) Representative protein array scans determining the content of soluble ligands secreted by donor or IPAH PAAF over 24 hours in cell culture medium. G) Heatmap of fold change expression of soluble ligands secreted by IPAH PAAF compared to donor PAAF (n=4 for each condition). H) Gene expression changes of cell state markers in donor and IPAH PASMC (n=6) treated 24h with pentraxin-3 (5  $\mu$ g/mL) or hepatocyte growth factor (HGF, 25 ng/mL). Smooth muscle myosin heavy chain: MHY11. Friedman test followed by Dunn's multiple comparisons test (\*p<0.05).

## Experimental Procedures

### *Human tissue samples*

Human lung samples from IPAH patients and downsized non-transplanted donor lungs, serving as healthy control, were obtained from Division of Thoracic Surgery, Medical University of Vienna, Austria. The protocol and tissue usage was approved by the local ethics committee (976/2010; 1417/2022) and patient consent was obtained before lung transplantation. Small size, resistance pulmonary arteries (diameter < 0.5 cm) were dissected from the lungs and used for smooth muscle cell and fibroblast cell isolation or flash-frozen in liquid nitrogen. Briefly, adventitial layer was pulled off the PA and used for outgrowth of PAAF. Remaining PA was cut open, endothelial layer scraped off and remaining media mechanically cut into small size pieces and used for smooth muscle cell outgrowth. Cells were grown in full media (VascuLife SMC or FibroLife S2, LifeLine Cell Technology) and used up to passage four. Respective basal media without added supplements and serum was used for starvation. Expression profiling (transcriptomic and proteomic) and functional cellular assays were performed on cells isolated from the same pulmonary artery. Histological staining of formalin-fixed paraffin-embedded human lung samples (n=5-10) included same control/patient cases that were used for in vitro studies. Frozen PA used for glysoaminoglycan measurement (n=8 for each condition) consisted of an independent control/patient cohort. Clinical data is given in Table S1.

### *Genome-wide expression profiling*

Briefly, whole genome expression profiling was performed on total RNA isolated using RNeasy Mini kit (Peqlab) from PAAF and PASMC in first passage (4 healthy donors and 4 IPAHs). Purified total RNA was amplified and Cy3-labeled using the LIRAK kit (Agilent) following the kit instructions. Per reaction, 200 ng of total RNA was used. The SureTag DNA labelling kit (Agilent, Waldbronn, Germany) was used to Cy5- and Cy3-label the samples and subsequently hybridized to 60-mer oligonucleotide spotted microarray slides (Agilent Human G3 8x60k, Design ID 072363). The following hybridization, washing, and drying steps were performed following the Agilent hybridisation protocol. Thereafter, the slides were scanned at 2  $\mu$ m/pixel resolution using the InnoScan 900 (Innopsys, Carbone, France). Image analysis was performed with Mapix 6.5.0 software, and calculated values for all spots were saved as GenePix results files. Stored data were evaluated using the R software (R Development Core Team 2007) and the limma package (Smyth, 2005) from BioConductor (Gentleman et al., 2004). Log mean spot signals were taken for further analysis. Data

was background corrected using the NormExp procedure on the negative control spots and quantile-normalized before averaging (Smyth and Speed, 2003). Genes were ranked for differential expression using a moderated t-statistic (Smyth, 2004). Results were uploaded to the National Center of Biotechnology Information Gene Expression Omnibus database (accession number GSE255669). List of differentially expressed genes is given in Data S1.

### *Proteomic Analysis*

Protein samples from isolated PASMC and PAAF were digested overnight at 37°C with Trypsin/LysC (Promega). Proteolytic digestion was quenched with 1% formic acid. The dried peptides were dissolved in reconstitution buffer (2% acetonitrile + 0.1% formic acid) and equimolar amounts (based on starting total protein concentration) of sample injected into the mass spectrometry instrument. Experiments were performed on the Orbitrap Fusion Tribrid mass spectrometer (Thermo Scientific) coupled with ACQUITY M-Class ultra-performance liquid chromatography (UPLC, Waters Corporation). A flow rate of 450 nL/min was used for this Liquid Chromatography/Mass Spectrometry experiment, where mobile phase A was 0.2% formic acid in water and mobile phase B was 0.2% formic acid in acetonitrile. Analytical columns were pulled using fused silica (I.D. 100 microns) and packed with Magic 1.8-micron 120Å UChrom C18 stationary phase (nanoLCMS Solutions) to a length of ~25 cm. Peptides were directly injected onto the analytical column using a gradient (2-45% B, followed by a high-B wash) of 80 minutes. The MS was operated in data-dependent fashion using CID (collision induced dissociation) for generating MS/MS spectra, collected in the ion trap. Raw data was processed using Byonic v3.2.0 (ProteinMetrics) to infer protein isoforms using the Uniprot Homo sapiens database. Proteolysis with Trypsin/LysC was assumed to be semi-specific allowing for N-ragged cleavage with up to 2 missed cleavage sites. Precursor mass accuracies were held within 12 ppm and 0.4 Da for MS/MS fragments. Proteins were held to a false discovery rate (FDR) of 1% or lower, using standard target-decoy approaches and only the proteins with >3 spectral counts were selected for further data processing (keratins and KAPs were removed at this stage). List of detected proteins is given in Data S2.

*Gene/Protein and pathway-centered functional data exploration and graphical representation*

Gene Set Enrichment Analysis (GSEA) and Over- Representation analysis (ORA) of transcriptomics and proteomics data was performed by using GO dataset (Mi et al., 2019) or BioPlanet (Huang et al., 2019) and applying the indicated significance and LFC cutoffs. The STRING (Version 11.0) Protein-Protein Interaction Networks/Functional Enrichment Analysis database was used to retrieve data on gene/protein interactions and examine the connections between genes. The gene-list enrichment tool Enrichr (Chen et al., 2013) was utilized to compare functional results. The open-source software platform Cytoscape (Version 3.7.2) was used for visualizing complex networks and representation of pathway terms with root nodes. Furthermore, RStudio (Version 1.1.383) and the package for circular visualization (Gu et al., 2014) and ggplot package (Wickham, 2016) were used for creating the circular plots.

#### *Multiplex immunofluorescent, RNA in situ hybridization and TUNEL staining*

Formalin-fixed, paraffin-embedded lung sections were deparaffinized, rehydrated and subjected to heat induced antigen retrieval. Multiplex immunofluorescence staining was done using Opal kit (Akoya). Successive rounds of primary antibody, detection reagent (Opal Polymer HRP, Akoya or Immpress HRP Polymer, Vector Labs) and fluorescent signal development (Opal dyes, Akoya or CF tyramide dye, Biotium), followed by antibody removal were performed according to manufacturer's instructions. List of antibodies is given in Table S2. DAPI (Thermo Scientific) was used as a nuclear counterstain at 2.5  $\mu$ g/mL final concentration. In the case of single molecule RNA in situ hybridization, slides were first against anti-PDGFR $\alpha$  antibody and processed further for RNA in situ hybridization according to manufacturer's instructions using RNAscope Multiplex Fluorescent V2 assay (ACD). Hybridization probes against human IGFBP5, SCARA5 and CFD were obtained from ACD. Similarly, upon PDGFR $\alpha$  detection and proteinase K treatment, DNA cleavage in apoptotic cells was detected using the terminal deoxynucleotidyl transferase (TdT)-mediated dUTP nick-end labeling (TUNEL) method according to manufacturer's instructions (Biotium). Following hybridization and TUNEL signal detection, slides were incubated with primary labelled antibody against alpha smooth muscle actin and counterstained with DAPI. Slides were imaged using SP8 fluorescence confocal microscope (Leica) and apochromatic glycerol immersion objectives 40x (1.25 numerical aperture).

#### *SeaHorse metabolic flux measurements*

Isolated PASMC and PAAF (20'000/well) were plated directly into Seahorse XF96 cell culture microplates (Agilent Technologies) and allowed to reach confluence. After 96 and 120 hours the medium was replaced by Standard Oxidation Stress Test assay medium (10 mM Glucose, 1mM Pyruvate, 2mM Glutamine) and plates were incubated in a non-CO<sub>2</sub> incubator for 60 minutes prior to the assay. Oxygen consumption rate (OCR) and extracellular acidification rate (ECAR) were measured in a Seahorse XFe96 extracellular flux analyzer (Agilent) using XF Substrate Oxidation Stress Test Kits (XF Long Chain Fatty Acid Oxidation Stress Test Kit, XF Glucose/Pyruvate Oxidation Stress Test Kit). First, basal respiration was established, followed by injection of the relevant pathway inhibitor (4  $\mu$ M etoxomir, 2  $\mu$ M UK5099). The response to the inhibitor was monitored, then ATP production was blocked by oligomycin (1.5  $\mu$ M), followed by the dissipation of proton gradients with FCCP (1  $\mu$ M). The electron transport chain was inhibited by rotenone/antimycin (0.5  $\mu$ M) to reveal the non-mitochondrial respiration. OCR/ECAR values are representing the ratio of Mitochondrial Respiration/Glycolysis derived from the first rate measurements of the Substrate Oxidation Stress Test. The acute response to the inhibitor represents alterations of basal respiration as OCR response to pathway inhibitors (etoxomir, UK5099). The glycolytic capacity was calculated as the difference of maximum ECAR measurement after oligomycin injection and the last ECAR measurement right before oligomycin injection. Non-mitochondrial respiration was defined as the minimum OCR measurement after rotenone/antimycin injection. Proton leak was calculated as minimum OCR measurement after oligomycin injection minus non-mitochondrial respiration. Measurements were performed as septuplets, rate measurement values from each well were normalized to their corresponding protein amounts. Data were analyzed using the Wave Software (Agilent Technologies, Version-2.6.1).

#### *Proteoglycan/Glycosaminoglycan quantification*

Glycosaminoglycans were quantified in isolated cryo-preserved PA of donor and IPAH patients as described previously (Dey et al., 1992). Briefly, isolated PA were weighed and digested overnight at 60°C in a phosphate-EDTA buffer papain solution. Resulting lysate was mixed with 1,9-dimethylmethylene blue assay and the absorbance of the resulting complex measured spectrophotometrically at 525 nm. Chondroitin sulphate was used for standard curve preparation. Combination of Alcian blue and Verhoeff's staining of formalin-fixed, paraffin-embedded lung sections was used for localization of glycosaminoglycans and elastic fibers, respectively. Quantitative image analysis of Alcian blue staining was performed on digitalized tissue

sections (VS200 Research Slide Scanner, Olympus Life Science) in QuPath software (<https://qupath.github.io/>, Version 0.5.1) (Bankhead et al., 2017). Each identifiable pulmonary artery on the slide was annotated into adventitial, medial and neointimal region of interest and for each region a median optical density (OD) measured using “add intensity features” function. Absolute OD value for each region of each vessel is expressed relative to mean OD calculated from the donor medial regions.

#### *Cellular turnover measurements*

Proliferation of PASMC and PAAF was determined by [<sup>3</sup>H]thymidine incorporation assay (BIOTREND Chemikalien, Germany). 7500 cells per well were seeded in a 96 well plate. The cells were starved in basal medium (without supplement) overnight and next day they were stimulated with 2% FCS or maintained in media without supplements as controls. Following 24h [<sup>3</sup>H]thymidine incorporation measurement was evaluated in each well. Alternatively, cell turnover in different passages was done by plating 100'000 cells in a flask and allowed to grow for 72 hours. Cells were detached by trypsinization and cell number were determined using Neubauer cell counting chamber.

#### *Mitochondrial content, membrane potential and cellular ROS*

Cellular reactive oxygen species (ROS) production was based on fluorescent imaging of the ROS indicator CellRox Deep Red (Thermo Scientific). Cells were loaded with 5µM of CellROX dye for 1 hour at 37°C, followed by confocal fluorescence imaging (LSM 510 Meta with a Plan Neofluar 40x/1.3 oil-immersion objective, Carl Zeiss) before and after stimulation with 50 ng/mL PDGF-BB (R&D Systems) for 40 minutes at 37°C. Mitochondrial membrane potential was measured in quench/de-quench mode following staining with 1 µM TMRM dye (Sigma Aldrich). Image analysis was performed in ImageJ (NIH). A binary image of the TMRM signal was created, to measure the cell area covered by mitochondria. Mitochondrial density was then determined by dividing the cell area with the area covered with mitochondria. Mitochondrial membrane potential was calculated by normalizing the TMRM signal to the mitochondrial density.

#### *RNA isolation and quantitative real-time polymerase chain reaction (qRT-PCR)*

Total RNA from PAAF and PASMC was extracted using peqGOLD Total RNA Kit (Peqlab) or innuPREP RNA Mini Kit (IST Innuscreen). The cDNA was reverse transcribed using a qScript cDNA Synthesis kit

(QuantaBio). Quantitative real-time polymerase chain reaction (qRT-PCR) was performed using the S'Green qPCR kit (Biozym) on LightCycler 480 (Roche Applied Science). The threshold cycle difference ( $\Delta CT$ ) was calculated using the equation  $\Delta CT = ([CT(B2M)+CT(HMBS)]/2) - CT(\text{Gene of Interest})$ . Beta-2-microglobulin (B2M) and hydroxymethylbilane synthase (HMBS) were used as reference genes. The primer list is given in Table S3.

#### *Adhesion and gap closure assays*

Adhesion assay was performed on Biocoat collagen I and laminin coated 24-well plates (Corning). Briefly, 50'000 cells were allowed to attach for 40 min at 37°C, followed by PBS wash, formalin fixation and staining with crystal violet. Images were transformed into 8-bit image type and the adhered cells were counted with the plugin in cell counter of the Fiji-Image J. Gap closure assay was performed in two chamber silicon inserts with a defined cell-free gap were used (Ibidi). Each chamber seeded with 15'000 cells that were allowed to grow till confluence. Experiment was started by removing the insert and image of the cell-free gap taken ( $t=0$ ). Subsequent images of the gap were taken 4, 8, 24 and 48 hours after removal of the insert. Analysis of wound area has been performed with Fiji-ImageJ. Briefly, the wound area of each picture was first identified with the MRI Wound healing tool and the area enclosed was then measured.

#### *Cell stimulations and co-culture experiment*

PASMC were cultured in 24well or 6well plates up to 90% confluence and serum starved for 24 hours. Cells were stimulated for 24 hours with ligands C3a (R&D Systems, 100 ng/mL), C5a (R&D Systems, 100 ng/mL), pentraxin-3 (R&D Systems, 5  $\mu$ g/mL), hepatocyte growth factor (Peprotech, 25 ng/mL), Chitinase 3-like 1 Protein (R&D Systems, 300 ng/mL), Insulin-like growth factor binding protein-3 (R&D Systems, 300 ng/mL), and Angiogenin (Biomol, 300 ng/mL) in starvation medium. Following stimulation, cells were washed with PBS and lysed for subsequent RNA isolation. For PAAF-PASMC co-culture experiment, cells were fluorescently labelled with either CellTracker Green CMFDA (Thermo Scientific) or CellTracker Red CMTPX (Thermo Scientific) for 30 min at 37°C. Labelled cells were trypsinized and plated in a 1:1 ratio (PAAF:PASMC) in a 6well plate in fully supplemented smooth muscle cell medium for 24 hours. Next day, cells were detached and single cell suspension processed for two-way fluorescence activated cell sorting. CMFDA and CMTPX viable cells (Sytox Blue dead cell stain negative cells) were sorted using FACSaria IIIu (BD Biosciences) at

the flow cytometry core facility (Center for Medical Research, Medical University of Graz). Collected cells were centrifuged and processed for RNA isolation. One part of RNA was used for qRT-PCR, while other RNA was used for bulk RNA sequencing analysis. Briefly, libraries were prepared using NEB Next® Ultra II RNA Library Prep Kit for Illumina (New England Biolabs) with rRNA Depletion kit v2 (Human/Mouse/Rat) (New England Biolabs) and sequenced upon library pooling on NovaSeq 6000 (Illumina). Results were uploaded to the National Center of Biotechnology Information Gene Expression Omnibus database (accession number GSE262069). List of differentially expressed genes is given in Data S4.

#### *Cell-cell communication analysis*

Ligand-receptor expression analysis was performed on previously published single cell RNA sequencing dataset of human pulmonary arteries from donors and PAH patients GSE210248 (Crnkovic et al., 2022). For the analysis, the data matrix was transformed into a Seurat object and was processed with the Seurat package (Version 4.3.0) (Butler et al., 2018) in the R studio environment (Version 4.1.2). The 10x files were converted into a Seurat object with CreateSeuratobject. Doublets were filtered out with the scDblFinder tool. Furthermore, all cells with more than 5% mitochondrial DNA (mtDNA) and cells with under 200 and over 2500 RNA counts were filtered out. Final quality control step included filtering out outliers defined as cells with an RNA-count outside the range of 5 MADs. Data normalization was performed with the NormalizeData function from Seurat, followed by data scaling (ScaleData). The FindVariableFeatures Seurat-function detected the variable features in the data set (selection method=vst, nfeatures=2000). A principal component analysis was run on the normalized and scaled data. The number of PC was set after plotting an elbow plot which showed an elbow between 20 and 30 clusters. The following steps included data integration with harmony (Version 0.1.1) and Uniform manifold Approximation (UMAP) depiction of the data (RunUMAP). The data was clustered with the help of the FindNeighbours- and FindClusters function. The cluster annotation to cell type was done manually based on gene enrichment of canonical cell type marker genes.

For the cell-cell-communication analysis the clustered datasets were normalized so that the number of cells per cell type in each group (PAH or donor) were comparable. Two independent analysis methods were used. A comparative Nichenet analysis was performed according to the Nichenet method (<https://github.com/saeyslab/nichenetr>, Version 2.0.4) (Browaeys et al., 2020). Donor and PAH niches were defined and smooth muscle cells and fibroblasts were each set as sender and receiver cell type. The analysis

was performed twice to obtain results for communication in both directions. CellChat analysis: A descriptive analysis of cell-cell-communication for donor and PAH samples was performed according to the CellChat tool ((<https://github.com/sqjin/CellChat>, Version 1.6.1) (Jin et al., 2021). The Seurat object was subset, and the analysis was performed separately for each subset.

### *Secretome analysis*

Proteome Profiler Human XL Cytokine Array Kit (R&D Systems) and Proteome Profiler Human Adipokine Array Kit (R&D Systems) were used to measure factors secreted by donor and IPAH PAAF. Briefly, PAAF were grown till 80-90% confluence and after 3-4 days medium was collected, centrifuged at 4°C, 400g for 5 min, aliquoted and stored at -80°C till measurement. Equal volume of cell culture supernatant was used in Proteome Profiler Array Kits and assay performed according to manufacturer's instructions. Signal intensity values for each spot were normalized to the mean value of the positive control spots for each membrane. Normalized intensity values were then used to calculate pairwise (IPAH-to-donor) relative expressions for each factor above the detection limit. In total, 4 such pairwise comparisons were done. We took into further consideration only those factors whose relative normalized expression levels changed by more than 10% in at least two pairwise comparisons. Obtained list of ligands with corresponding normalized relative expressions were hierarchically clustered using Clustergrammer online tool (Fernandez et al., 2017) to provide a heatmap and correlation matrix visualization.

### *Statistical analysis*

Graphs and statistical calculations were performed using GraphPad Prism (Version 8.0, GraphPad Software) or R (v3.5.3, packages stringr, data.table, readxl, openxlsx, MetaboAnalystR, ggplot2, colorspace, circlize) and Tibco Spotfire (v11.1.0). Probability values of  $p < 0.05$  were considered statistically significant. Differences between groups were investigated using Student's t test, Mann-Whitney or Friedman test. 2-way or 3-way ANOVA was used for interaction analysis. For orthogonal PLS-DA (OPLS-DA) data was filtered to retain only features with less than 30% missing data (proteomics 1552 genes, transcriptomics 23541 genes). OPLS-DA was performed centered and scaled to unit variance with a standard 7-fold cross validation for the classification factor. Model stability was additionally verified with 1000 random label permutations and models with  $Q2 > 50\%$  were considered significant.

## References

Angueira AR, Sakers AP, Holman CD, Cheng L, Arbocco MN, Shamsi F, Lynes MD, Shrestha R, Okada C, Batmanov K, Susztak K, Tseng Y-H, Liaw L, Seale P. 2021. Defining the lineage of thermogenic perivascular adipose tissue. *Nat Metab* **3**:469–484. doi:10.1038/s42255-021-00380-0

Bankhead P, Loughrey MB, Fernández JA, Dombrowski Y, McArt DG, Dunne PD, McQuaid S, Gray RT, Murray LJ, Coleman HG, James JA, Salto-Tellez M, Hamilton PW. 2017. QuPath: Open source software for digital pathology image analysis. *Sci Rep* **7**:16878. doi:10.1038/s41598-017-17204-5

Barnes JW, Tian L, Heresi GA, Farver CF, Asosingh K, Comhair SAA, Aulak KS, Dweik RA. 2015. O-linked  $\beta$ -N-acetylglucosamine transferase directs cell proliferation in idiopathic pulmonary arterial hypertension. *Circulation* **131**:1260–1268. doi:10.1161/CIRCULATIONAHA.114.013878

Biasin V, Crnkovic S, Sahu-Osen A, Birnhuber A, El Agha E, Sinn K, Klepetko W, Olschewski A, Bellusci S, Marsh LM, Kwapiszewska G. 2020. PDGFR $\alpha$  and  $\alpha$ SMA mark two distinct mesenchymal cell populations involved in parenchymal and vascular remodeling in pulmonary fibrosis. *Am J Physiol Lung Cell Mol Physiol* **318**:L684–L697. doi:10.1152/ajplung.00128.2019

Bordenave J, Tu L, Berrebeh N, Thuillet R, Cumont A, Le Vely B, Fadel E, Nadaud S, Savale L, Humbert M, Huertas A, Guignabert C. 2020. Lineage Tracing Reveals the Dynamic Contribution of Pericytes to the Blood Vessel Remodeling in Pulmonary Hypertension. *Arterioscler Thromb Vasc Biol* **40**:766–782. doi:10.1161/ATVBAHA.119.313715

Browaeys R, Saelens W, Saeys Y. 2020. NicheNet: modeling intercellular communication by linking ligands to target genes. *Nat Methods* **17**:159–162. doi:10.1038/s41592-019-0667-5

Buse MG. 2006. Hexosamines, insulin resistance, and the complications of diabetes: current status. *Am J Physiol Endocrinol Metab* **290**:E1–E8. doi:10.1152/ajpendo.00329.2005

Butler A, Hoffman P, Smibert P, Papalexi E, Satija R. 2018. Integrating single-cell transcriptomic data across different conditions, technologies, and species. *Nat Biotechnol* **36**:411–420. doi:10.1038/nbt.4096

Camozzi M, Zacchigna S, Rusnati M, Coltrini D, Ramirez-Correa G, Bottazzi B, Mantovani A, Giacca M, Presta M. 2005. Pentraxin 3 inhibits fibroblast growth factor 2-dependent activation of smooth muscle cells in vitro and neointima formation in vivo. *Arterioscler Thromb Vasc Biol* **25**:1837–1842. doi:10.1161/01.ATV.0000177807.54959.7d

Chang Y-T, Chan CK, Eriksson I, Johnson PY, Cao X, Westöö C, Norvik C, Andersson-Sjöland A, Westergren-Thorsson G, Johansson S, Hedin U, Kjellén L, Wight TN, Tran-Lundmark K. 2016. Versican accumulates in vascular lesions in pulmonary arterial hypertension. *Pulm Circ* **6**:347–359. doi:10.1086/686994

Chelladurai P, Kuenne C, Bourgeois A, Günther S, Valasarajan C, Cherian AV, Rottier RJ, Romanet C, Weigert A, Boucherat O, Eichstaedt CA, Ruppert C, Guenther A, Braun T, Looso M, Savai R, Seeger W, Bauer U-M, Bonnet S, Pullamsetti SS. 2022. Epigenetic reactivation of transcriptional programs orchestrating fetal lung development in human pulmonary hypertension. *Science Translational Medicine* **14**:eabe5407. doi:10.1126/scitranslmed.abe5407

Chen EY, Tan CM, Kou Y, Duan Q, Wang Z, Meirelles GV, Clark NR, Ma'ayan A. 2013. Enrichr: interactive and collaborative HTML5 gene list enrichment analysis tool. *BMC Bioinformatics* **14**:128. doi:10.1186/1471-2105-14-128

Chu X, Kheirollahi V, Lingampally A, Chelladurai P, Valasarajan C, Vazquez-Armendariz AI, Hadzic S, Khadim A, Pak O, Rivetti S, Wilhelm J, Bartkuhn M, Crnkovic S, Moiseenko A, Heiner M, Kraut S, Atefi LS, Koepke J, Valente G, Ruppert C, Braun T, Samakovlis C, Alexopoulos I, Looso M, Chao C-M, Herold S, Seeger W, Kwapiszewska G, Huang X, Zhang J-S, Pullamsetti SS, Weissmann N, Li X, El Agha E, Bellusci

S. 2024. GLI1+ Cells Contribute to Vascular Remodeling in Pulmonary Hypertension. *Circ Res* **134**:e133–e149. doi:10.1161/CIRCRESAHA.123.323736

Clark SJ, Bishop PN, Day AJ. 2013. The proteoglycan glycomatrix: a sugar microenvironment essential for complement regulation. *Front Immunol* **4**:412. doi:10.3389/fimmu.2013.00412

Crnkovic S, Marsh LM, El Agha E, Voswinckel R, Ghanim B, Klepetko W, Stacher-Prihse E, Olschewski H, Bloch W, Bellusci S, Olschewski A, Kwapiszewska G. 2018. Resident cell lineages are preserved in pulmonary vascular remodeling. *J Pathol* **244**:485–498. doi:10.1002/path.5044

Crnkovic S, Rittchen S, Jandl K, Gindlhuber J, Zabini D, Mutgan AC, Valzano F, Boehm PM, Hoetzenegger K, Toller W, Veith C, Heinemann A, Schermuly RT, Olschewski A, Marsh LM, Kwapiszewska G. 2023. Divergent Roles of Ephrin-B2/EphB4 Guidance System in Pulmonary Hypertension. *Hypertension* **80**:e17–e28. doi:10.1161/HYPERTENSIONAHA.122.19479

Crnkovic S, Valzano F, Fließer E, Gindlhuber J, Thekkakara Puthenparampil H, Basil M, Morley MP, Katzen J, Gschwandtner E, Klepetko W, Cantu E, Wolinski H, Olschewski H, Lindenmann J, Zhao Y-Y, Morrisey EE, Marsh LM, Kwapiszewska G. 2022. Single-cell transcriptomics reveals skewed cellular communication and phenotypic shift in pulmonary artery remodeling. *JCI Insight* **7**:e153471. doi:10.1172/jci.insight.153471

Dahlgren MW, Jones SW, Cautivo KM, Dubinin A, Ortiz-Carpena JF, Farhat S, Yu KS, Lee K, Wang C, Molofsky AV, Tward AD, Krummel MF, Peng T, Molofsky AB. 2019. Adventitial Stromal Cells Define Group 2 Innate Lymphoid Cell Tissue Niches. *Immunity* **50**:707-722.e6. doi:10.1016/j.jimmuni.2019.02.002

Dey P, Saphos CA, McDonnell J, Moore VL. 1992. Studies on the quantification of proteoglycans by the dimethylmethylene blue dye-binding method. Specificity, quantitation in synovial lavage fluid, and automation. *Connect Tissue Res* **28**:317–324. doi:10.3109/03008209209016823

El Kasmi KC, Pugliese SC, Riddle SR, Poth JM, Anderson AL, Frid MG, Li M, Pullamsetti SS, Savai R, Nagel MA, Fini MA, Graham BB, Tuder RM, Friedman JE, Eltzschig HK, Sokol RJ, Stenmark KR. 2014. Adventitial fibroblasts induce a distinct proinflammatory/profibrotic macrophage phenotype in pulmonary hypertension. *J Immunol* **193**:597–609. doi:10.4049/jimmunol.1303048

Fernandez NF, Gundersen GW, Rahman A, Grimes ML, Rikova K, Hornbeck P, Ma'ayan A. 2017. Clustergrammer, a web-based heatmap visualization and analysis tool for high-dimensional biological data. *Sci Data* **4**:170151. doi:10.1038/sdata.2017.151

Frid MG, McKeon BA, Thurman JM, Maron BA, Li M, Zhang H, Kumar S, Sullivan T, Laskowsky J, Fini MA, Hu S, Tuder RM, Gandjeva A, Wilkins MR, Rhodes CJ, Ghataorhe P, Leopold JA, Wang R-S, Holers VM, Stenmark KR. 2020. Immunoglobulin-driven Complement Activation Regulates Proinflammatory Remodeling in Pulmonary Hypertension. *Am J Respir Crit Care Med* **201**:224–239. doi:10.1164/rccm.201903-0591OC

Gentleman RC, Carey VJ, Bates DM, Bolstad B, Dettling M, Dudoit S, Ellis B, Gautier L, Ge Y, Gentry J, Hornik K, Hothorn T, Huber W, Iacus S, Irizarry R, Leisch F, Li C, Maechler M, Rossini AJ, Sawitzki G, Smith C, Smyth G, Tierney L, Yang JY, Zhang J. 2004. Bioconductor: open software development for computational biology and bioinformatics. *Genome Biology* **5**:R80. doi:10.1186/gb-2004-5-10-r80

Gomez D, Owens GK. 2012. Smooth muscle cell phenotypic switching in atherosclerosis. *Cardiovasc Res* **95**:156–164. doi:10.1093/cvr/cvs115

Gorr MW, Sriram K, Muthusamy A, Insel PA. 2020. Transcriptomic analysis of pulmonary artery smooth muscle cells identifies new potential therapeutic targets for idiopathic pulmonary arterial hypertension. *Br J Pharmacol* **177**:3505–3518. doi:10.1111/bph.15074

Gu Z, Gu L, Eils R, Schlesner M, Brors B. 2014. circlize Implements and enhances circular visualization in R. *Bioinformatics* **30**:2811–2812. doi:10.1093/bioinformatics/btu393

Hoffmann J, Marsh LM, Pieper M, Stacher E, Ghanim B, Kovacs G, König P, Wilkens H, Haitchi HM, Hoefer G, Klepetko W, Olschewski H, Olschewski A, Kwapiszewska G. 2015. Compartment-specific expression of collagens and their processing enzymes in intrapulmonary arteries of IPAH patients. *Am J Physiol Lung Cell Mol Physiol* **308**:L1002-1013. doi:10.1152/ajplung.00383.2014

Hoffmann J, Wilhelm J, Marsh LM, Ghanim B, Klepetko W, Kovacs G, Olschewski H, Olschewski A, Kwapiszewska G. 2014. Distinct differences in gene expression patterns in pulmonary arteries of patients with chronic obstructive pulmonary disease and idiopathic pulmonary fibrosis with pulmonary hypertension. *Am J Respir Crit Care Med* **190**:98–111. doi:10.1164/rccm.201401-0037OC

Hong Z, Chen K-H, DasGupta A, Potus F, Dunham-Snary K, Bonnet S, Tian L, Fu J, Breuils-Bonnet S, Provencher S, Wu D, Mewburn J, Ormiston ML, Archer SL. 2017. MicroRNA-138 and MicroRNA-25 Down-regulate Mitochondrial Calcium Uniporter, Causing the Pulmonary Arterial Hypertension Cancer Phenotype. *Am J Respir Crit Care Med* **195**:515–529. doi:10.1164/rccm.201604-0814OC

Höög J-O, Ostberg LJ. 2011. Mammalian alcohol dehydrogenases--a comparative investigation at gene and protein levels. *Chem Biol Interact* **191**:2–7. doi:10.1016/j.cbi.2011.01.028

Huang R, Grishagin I, Wang Y, Zhao T, Greene J, Obenauer JC, Ngan D, Nguyen D-T, Guha R, Jadhav A, Southall N, Simeonov A, Austin CP. 2019. The NCATS BioPlanet - An Integrated Platform for Exploring the Universe of Cellular Signaling Pathways for Toxicology, Systems Biology, and Chemical Genomics. *Front Pharmacol* **10**:445. doi:10.3389/fphar.2019.00445

Humbert M, Guignabert C, Bonnet S, Dorfmüller P, Klinger JR, Nicolls MR, Olschewski AJ, Pullamsetti SS, Schermuly RT, Stenmark KR, Rabinovitch M. 2019. Pathology and pathobiology of pulmonary hypertension: state of the art and research perspectives. *Eur Respir J* **53**:1801887. doi:10.1183/13993003.01887-2018

Jandl K, Marsh LM, Hoffmann J, Mutgan AC, Baum O, Bloch W, Thekkekara-Puthenparampil H, Kolb D, Sinn K, Klepetko W, Heinemann A, Olschewski A, Olschewski H, Kwapiszewska G. 2020. Basement Membrane Remodeling Controls Endothelial Function in Idiopathic Pulmonary Arterial Hypertension. *Am J Respir Cell Mol Biol* **63**:104–117. doi:10.1165/rcmb.2019-0303OC

Jin S, Guerrero-Juarez CF, Zhang L, Chang I, Ramos R, Kuan C-H, Myung P, Plikus MV, Nie Q. 2021. Inference and analysis of cell-cell communication using CellChat. *Nat Commun* **12**:1088. doi:10.1038/s41467-021-21246-9

Kokoszka JE, Coskun P, Esposito LA, Wallace DC. 2001. Increased mitochondrial oxidative stress in the Sod2 (+/−) mouse results in the age-related decline of mitochondrial function culminating in increased apoptosis. *Proc Natl Acad Sci U S A* **98**:2278–2283. doi:10.1073/pnas.051627098

Languino LR, Gehlsen KR, Wayner E, Carter WG, Engvall E, Ruoslahti E. 1989. Endothelial cells use alpha 2 beta 1 integrin as a laminin receptor. *J Cell Biol* **109**:2455–2462. doi:10.1083/jcb.109.5.2455

Li JY, Paragas N, Ned RM, Qiu A, Viltard M, Leete T, Drexler IR, Chen X, Sanna-Cherchi S, Mohammed F, Williams D, Lin CS, Schmidt-Ott KM, Andrews NC, Barasch J. 2009. Scara5 is a ferritin receptor mediating non-transferrin iron delivery. *Dev Cell* **16**:35–46. doi:10.1016/j.devcel.2008.12.002

Li M, Plecitá-Hlavatá L, Dobrinskikh E, McKeon BA, Gandjeva A, Riddle S, Laux A, Prasad RR, Kumar S, Tuder RM, Zhang H, Hu C-J, Stenmark KR. 2023. SIRT3 Is a Critical Regulator of Mitochondrial Function of Fibroblasts in Pulmonary Hypertension. *Am J Respir Cell Mol Biol* **69**:570–583. doi:10.1165/rcmb.2022-0360OC

Mi H, Muruganujan A, Ebert D, Huang X, Thomas PD. 2019. PANTHER version 14: more genomes, a new PANTHER GO-slim and improvements in enrichment analysis tools. *Nucleic Acids Res* **47**:D419–D426. doi:10.1093/nar/gky1038

Moiseeva EP. 2001. Adhesion receptors of vascular smooth muscle cells and their functions. *Cardiovascular Research* **52**:372–386. doi:10.1016/S0008-6363(01)00399-6

Muhl L, Genové G, Leptidis S, Liu J, He L, Mocci G, Sun Y, Gustafsson S, Buyandelger B, Chivukula IV, Segerstolpe Å, Raschperger E, Hansson EM, Björkegren JLM, Peng X-R, Vanlandewijck M, Lendahl U, Betsholtz C. 2020. Single-cell analysis uncovers fibroblast heterogeneity and criteria for fibroblast and mural cell identification and discrimination. *Nat Commun* **11**:3953. doi:10.1038/s41467-020-17740-1

Muhl L, Mocci G, Pietilä R, Liu J, He L, Genové G, Leptidis S, Gustafsson S, Buyandelger B, Raschperger E, Hansson EM, Björkegren JLM, Vanlandewijck M, Lendahl U, Betsholtz C. 2022. A single-cell transcriptomic inventory of murine smooth muscle cells. *Dev Cell* **57**:2426-2443.e6. doi:10.1016/j.devcel.2022.09.015

Mutgan AC, Radic N, Valzano F, Crnkovic S, El-Merhie N, Evermann M, Hoetzenrecker K, Foris V, Brcic L, Marsh LM, Tran-Lundmark K, Jandl K, Kwapiszewska G. 2024. A comprehensive map of proteoglycan expression and deposition in the pulmonary arterial wall in health and pulmonary hypertension. *Am J Physiol Lung Cell Mol Physiol* **327**:L173–L188. doi:10.1152/ajplung.00022.2024

Nguyen BP, Gil SG, Carter WG. 2000. Deposition of Laminin 5 by Keratinocytes Regulates Integrin Adhesion and Signaling\*. *Journal of Biological Chemistry* **275**:31896–31907. doi:10.1074/jbc.M006379200

Park CS, Kim SH, Yang HY, Kim J-H, Schermuly RT, Cho YS, Kang H, Park J-H, Lee E, Park H, Yang JM, Noh TW, Lee S-P, Bae SS, Han J, Ju YS, Park J-B, Kim I. 2022. Sox17 Deficiency Promotes Pulmonary Arterial Hypertension via HGF/c-Met Signaling. *Circ Res* **131**:792–806. doi:10.1161/CIRCRESAHA.122.320845

Paulin R, Dromparis P, Sutendra G, Gurtu V, Zervopoulos S, Bowers L, Haromy A, Webster L, Provencher S, Bonnet S, Michelakis ED. 2014. Sirtuin 3 deficiency is associated with inhibited mitochondrial function and pulmonary arterial hypertension in rodents and humans. *Cell Metab* **20**:827–839. doi:10.1016/j.cmet.2014.08.011

Plecitá-Hlavatá L, Brázdová A, Křivonosková M, Hu C-J, Phang T, Tauber J, Li M, Zhang H, Hoetzenrecker K, Crnkovic S, Kwapiszewska G, Stenmark KR. 2023. Microenvironmental regulation of T-cells in pulmonary hypertension. *Front Immunol* **14**:1223122. doi:10.3389/fimmu.2023.1223122

Régent A, Ly KH, Lofek S, Clary G, Tamby M, Tamas N, Federici C, Broussard C, Chafey P, Liaudet-Coopman E, Humbert M, Perros F, Mounthou L. 2016. Proteomic analysis of vascular smooth muscle cells in physiological condition and in pulmonary arterial hypertension: Toward contractile versus synthetic phenotypes. *Proteomics* **16**:2637–2649. doi:10.1002/pmic.201500006

Ruiter G, Lankhorst S, Boonstra A, Postmus PE, Zweegman S, Westerhof N, van der Laarse WJ, Vonk-Noordegraaf A. 2011. Iron deficiency is common in idiopathic pulmonary arterial hypertension. *Eur Respir J* **37**:1386–1391. doi:10.1183/09031936.00100510

Shankman LS, Gomez D, Cherepanova OA, Salmon M, Alencar GF, Haskins RM, Swiatlowska P, Newman AAC, Greene ES, Straub AC, Isakson B, Randolph GJ, Owens GK. 2015. KLF4 Dependent Phenotypic Modulation of SMCs Plays a Key Role in Atherosclerotic Plaque Pathogenesis. *Nat Med* **21**:628–637. doi:10.1038/nm.3866

Sheikh AQ, Misra A, Rosas IO, Adams RH, Greif DM. 2015. Smooth muscle cell progenitors are primed to muscularize in pulmonary hypertension. *Sci Transl Med* **7**:308ra159. doi:10.1126/scitranslmed.aaa9712

Short M, Nemenoff RA, Zawada WM, Stenmark KR, Das M. 2004. Hypoxia induces differentiation of pulmonary artery adventitial fibroblasts into myofibroblasts. *Am J Physiol Cell Physiol* **286**:C416-425. doi:10.1152/ajpcell.00169.2003

Sikkema L, Ramírez-Suástequi C, Strobl DC, Gillett TE, Zappia L, Madissoon E, Markov NS, Zaragozi L-E, Ji Y, Ansari M, Arguel M-J, Apperloo L, Banchero M, Bécavin C, Berg M, Chichelnitskiy E, Chung M-I, Collin A, Gay ACA, Gote-Schniering J, Hooshiar Kashani B, Inecik K, Jain M, Kapellos TS, Kole TM, Leroy S, Mayr CH, Oliver AJ, von Papen M, Peter L, Taylor CJ, Walzthoeni T, Xu C, Bui LT, De Donno C, Dony L, Faiz A, Guo M, Gutierrez AJ, Heumos L, Huang N, Ibarra IL, Jackson ND, Kadur Lakshminarasimha

Murthy P, Lotfollahi M, Tabib T, Talavera-López C, Travaglini KJ, Wilbrey-Clark A, Worlock KB, Yoshida M, Lung Biological Network Consortium, van den Berge M, Bossé Y, Desai TJ, Eickelberg O, Kaminski N, Krasnow MA, Lafyatis R, Nikolic MZ, Powell JE, Rajagopal J, Rojas M, Rozenblatt-Rosen O, Seibold MA, Sheppard D, Shepherd DP, Sin DD, Timens W, Tsankov AM, Whitsett J, Xu Y, Banovich NE, Barbry P, Duong TE, Falk CS, Meyer KB, Kropski JA, Pe'er D, Schiller HB, Tata PR, Schultze JL, Teichmann SA, Misharin AV, Nawijn MC, Luecken MD, Theis FJ. 2023. An integrated cell atlas of the lung in health and disease. *Nat Med* **29**:1563–1577. doi:10.1038/s41591-023-02327-2

Smyth GK. 2005. limma: Linear Models for Microarray Data In: Gentleman R, Carey VJ, Huber W, Irizarry RA, Dudoit S, editors. *Bioinformatics and Computational Biology Solutions Using R and Bioconductor, Statistics for Biology and Health*. New York: Springer-Verlag. pp. 397–420. doi:10.1007/0-387-29362-0\_23

Smyth GK. 2004. Linear models and empirical bayes methods for assessing differential expression in microarray experiments. *Stat Appl Genet Mol Biol* **3**:Article3. doi:10.2202/1544-6115.1027

Smyth GK, Speed T. 2003. Normalization of cDNA microarray data. *Methods* **31**:265–273. doi:10.1016/s1046-2023(03)00155-5

Snider P, Fix JL, Rogers R, Peabody-Dowling G, Ingram D, Lilly B, Conway SJ. 2008. Generation and characterization of Csrp1 enhancer-driven tissue-restricted Cre-recombinase mice. *Genesis* **46**:167–176. doi:10.1002/dvg.20379

Stacher E, Graham BB, Hunt JM, Gandjeva A, Groshong SD, McLaughlin VV, Jessup M, Grizzle WE, Aldred MA, Cool CD, Tuder RM. 2012. Modern age pathology of pulmonary arterial hypertension. *Am J Respir Crit Care Med* **186**:261–272. doi:10.1164/rccm.201201-0164OC

Steffes LC, Froistad AA, Andruska A, Boehm M, McGlynn M, Zhang F, Zhang W, Hou D, Tian X, Miquerol L, Nadeau K, Metzger RJ, Spiekerkoetter E, Kumar ME. 2020. A Notch3-Marked Subpopulation of Vascular Smooth Muscle Cells Is the Cell of Origin for Occlusive Pulmonary Vascular Lesions. *Circulation* **142**:1545–1561. doi:10.1161/CIRCULATIONAHA.120.045750

Stenmark KR, Frid MG, Graham BB, Tuder RM. 2018. Dynamic and diverse changes in the functional properties of vascular smooth muscle cells in pulmonary hypertension. *Cardiovasc Res* **114**:551–564. doi:10.1093/cvr/cvy004

Sutendra G, Bonnet S, Rochefort G, Haromy A, Folmes KD, Lopaschuk GD, Dyck JRB, Michelakis ED. 2010. Fatty acid oxidation and malonyl-CoA decarboxylase in the vascular remodeling of pulmonary hypertension. *Sci Transl Med* **2**:44ra58. doi:10.1126/scitranslmed.3001327

Thenappan T, Chan SY, Weir EK. 2018. Role of extracellular matrix in the pathogenesis of pulmonary arterial hypertension. *Am J Physiol Heart Circ Physiol* **315**:H1322–H1331. doi:10.1152/ajpheart.00136.2018

Travaglini KJ, Nabhan AN, Penland L, Sinha R, Gillich A, Sit RV, Chang S, Conley SD, Mori Y, Seita J, Berry GJ, Shrager JB, Metzger RJ, Kuo CS, Neff N, Weissman IL, Quake SR, Krasnow MA. 2020. A molecular cell atlas of the human lung from single-cell RNA sequencing. *Nature* **587**:619–625. doi:10.1038/s41586-020-2922-4

Viswanathan G, Kirshner HF, Nazo N, Ali S, Ganapathi A, Cumming I, Zhuang Y, Choi I, Warman A, Jassal C, Almeida-Peters S, Haney J, Corcoran D, Yu Y-R, Rajagopal S. 2023. Single-Cell Analysis Reveals Distinct Immune and Smooth Muscle Cell Populations that Contribute to Chronic Thromboembolic Pulmonary Hypertension. *Am J Respir Crit Care Med* **207**:1358–1375. doi:10.1164/rccm.202203-0441OC

Wang X, Adams LD, Pabón LM, Mahoney WM, Beaudry D, Gunaje J, Geary RL, Deblois D, Schwartz SM. 2008. RGS5, RGS4, and RGS2 expression and aortic contractility are dynamically co-regulated during aortic banding-induced hypertrophy. *J Mol Cell Cardiol* **44**:539–550. doi:10.1016/j.yjmcc.2007.11.019

White RT, Damm D, Hancock N, Rosen BS, Lowell BB, Usher P, Flier JS, Spiegelman BM. 1992. Human adipsin is identical to complement factor D and is expressed at high levels in adipose tissue. *J Biol Chem* **267**:9210–9213.

Wickham H. 2016. *ggplot2, Use R!* Cham: Springer International Publishing. doi:10.1007/978-3-319-24277-4

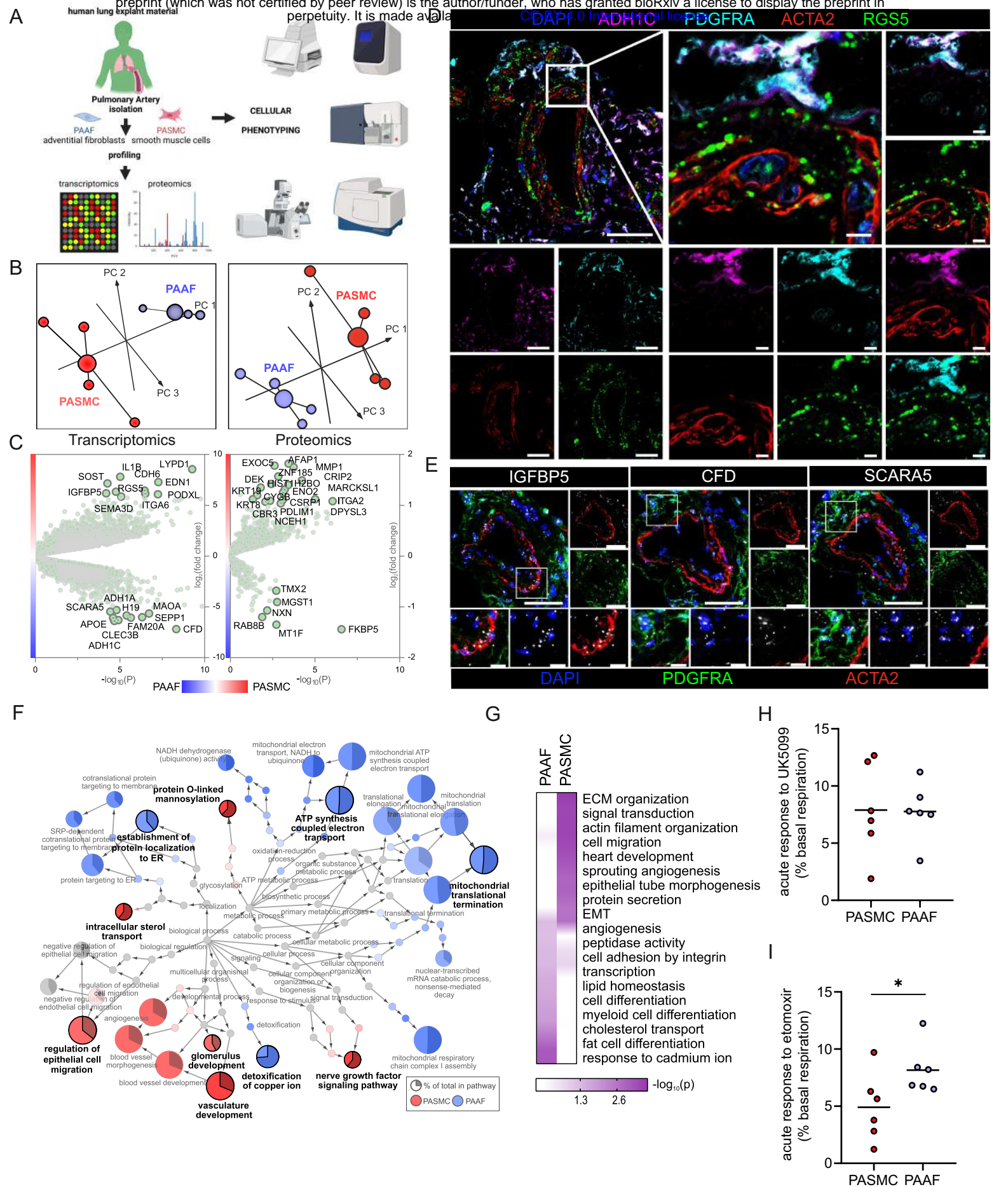
Wight TN, Merrilees MJ. 2004. Proteoglycans in atherosclerosis and restenosis: key roles for versican. *Circ Res* **94**:1158–1167. doi:10.1161/01.RES.0000126921.29919.51

Wirka RC, Wagh D, Paik DT, Pjanic M, Nguyen T, Miller CL, Kundu R, Nagao M, Coller J, Koyano TK, Fong R, Woo YJ, Liu B, Montgomery SB, Wu JC, Zhu K, Chang R, Alamprese M, Tallquist MD, Kim JB, Quertermous T. 2019. Atheroprotective roles of smooth muscle cell phenotypic modulation and the TCF21 disease gene as revealed by single-cell analysis. *Nat Med* **25**:1280–1289. doi:10.1038/s41591-019-0512-5

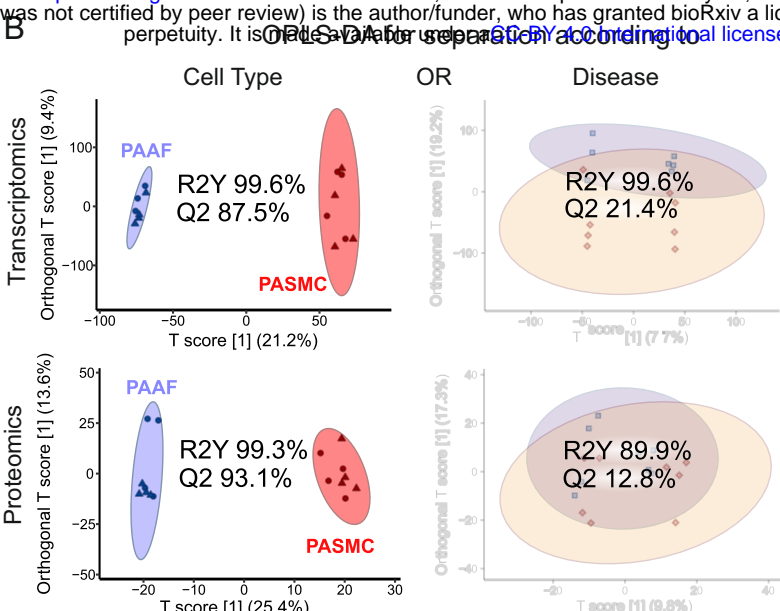
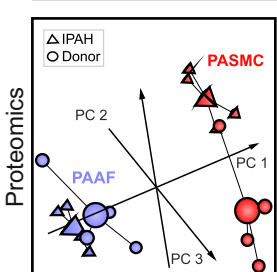
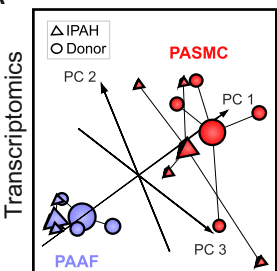
Worssam MD, Lambert J, Oc S, Taylor JCK, Taylor AL, Dobnikar L, Chappell J, Harman JL, Figg NL, Finigan A, Foote K, Uryga AK, Bennett MR, Spivakov M, Jørgensen HF. 2023. Cellular mechanisms of oligoclonal vascular smooth muscle cell expansion in cardiovascular disease. *Cardiovasc Res* **119**:1279–1294. doi:10.1093/cvr/cvac138

Zhang H, Li M, Hu C-J, Stenmark KR. 2024. Fibroblasts in Pulmonary Hypertension: Roles and Molecular Mechanisms. *Cells* **13**:914. doi:10.3390/cells13110914

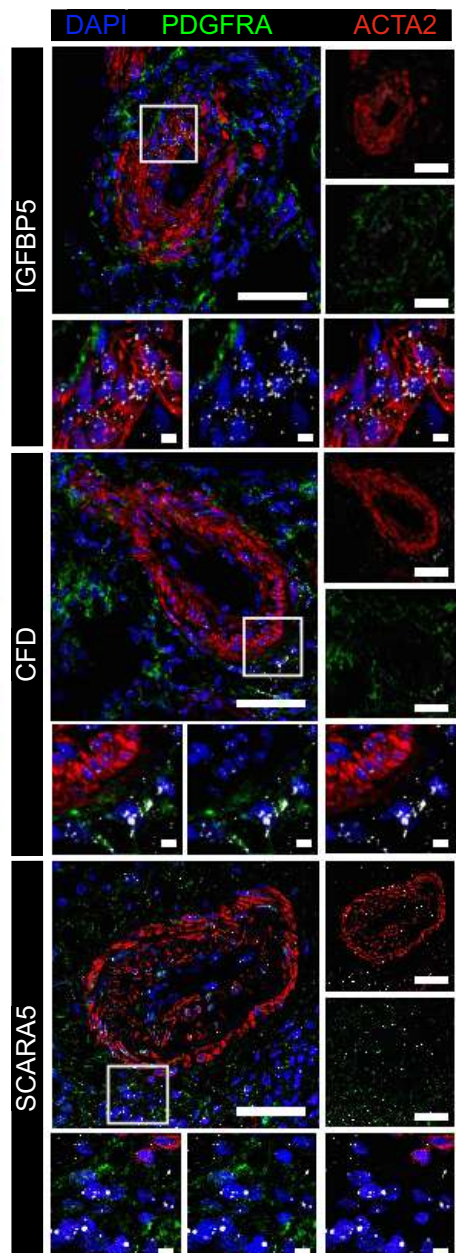
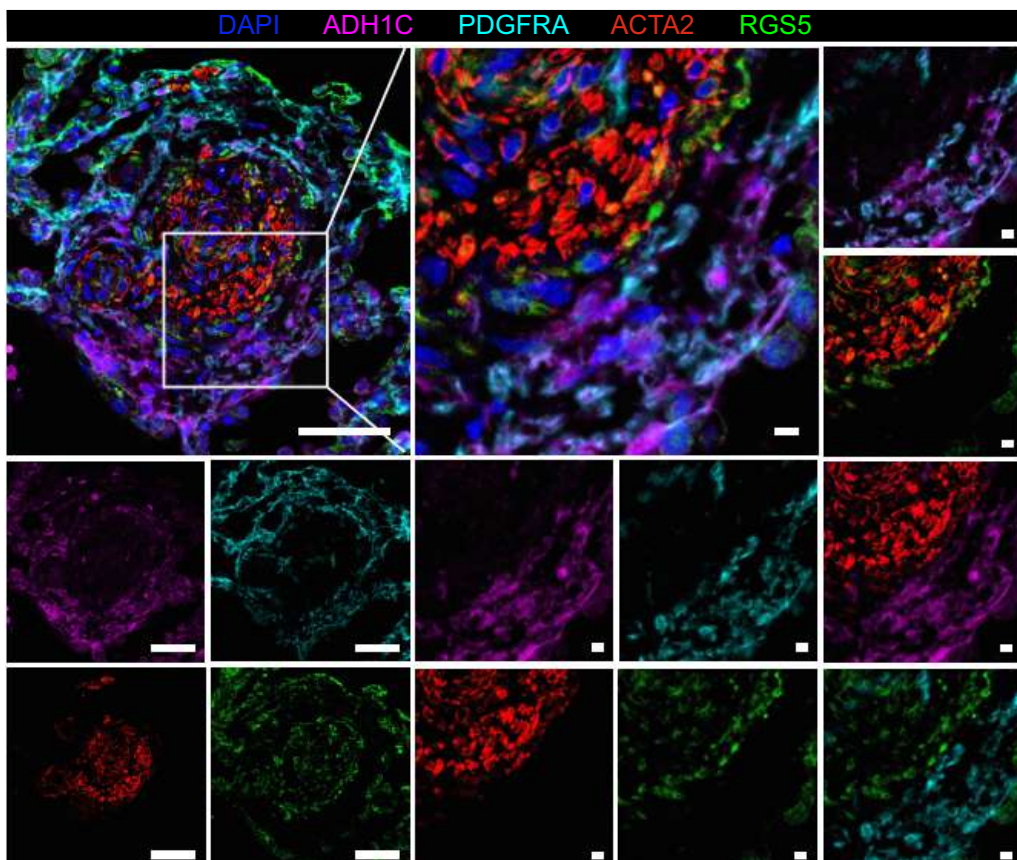
Zhang H, Wang D, Li M, Plecitá-Hlavatá L, D'Alessandro A, Tauber J, Riddle S, Kumar S, Flockton A, McKeon BA, Frid MG, Reisz JA, Caruso P, El Kasmi KC, Ježek P, Morrell NW, Hu C-J, Stenmark KR. 2017. Metabolic and Proliferative State of Vascular Adventitial Fibroblasts in Pulmonary Hypertension Is Regulated Through a MicroRNA-124/PTBP1 (Polypyrimidine Tract Binding Protein 1)/Pyruvate Kinase Muscle Axis. *Circulation* **136**:2468–2485. doi:10.1161/CIRCULATIONAHA.117.028069



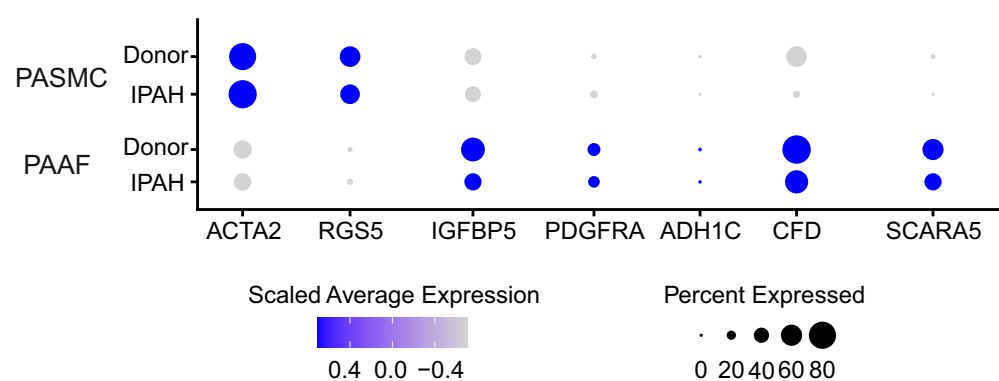
A



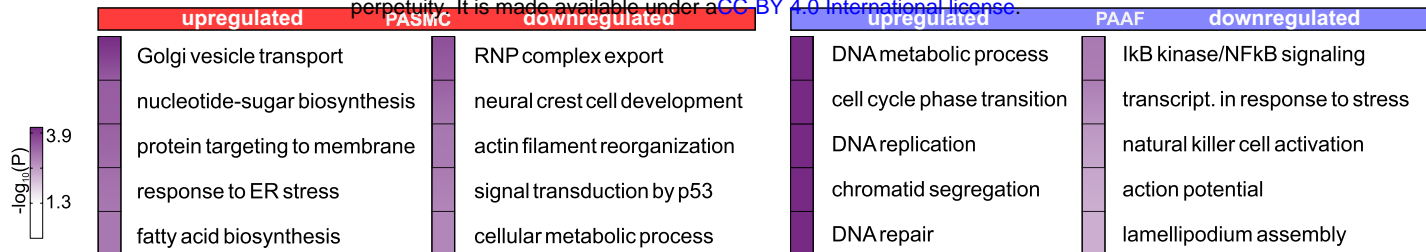
D



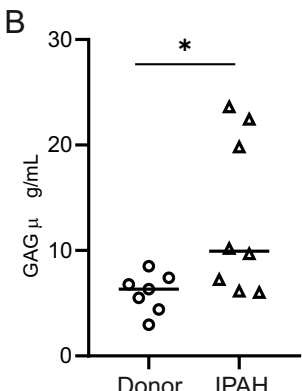
E



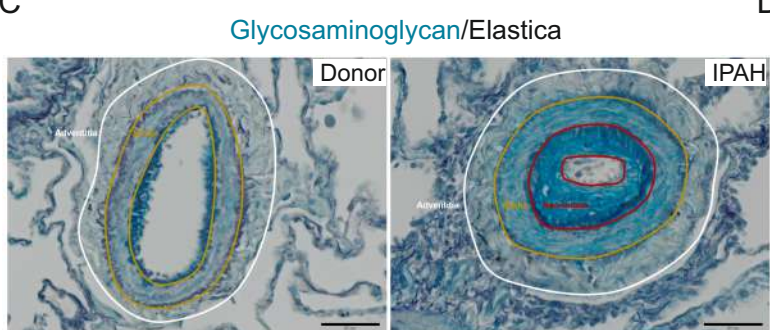
A



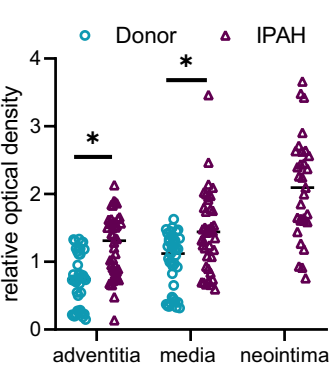
B



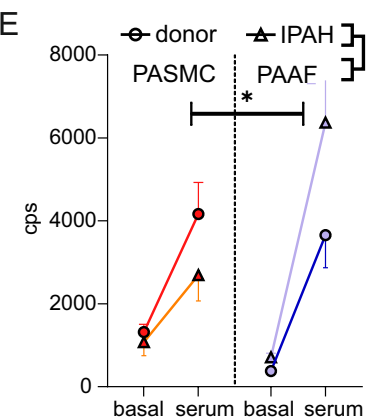
C



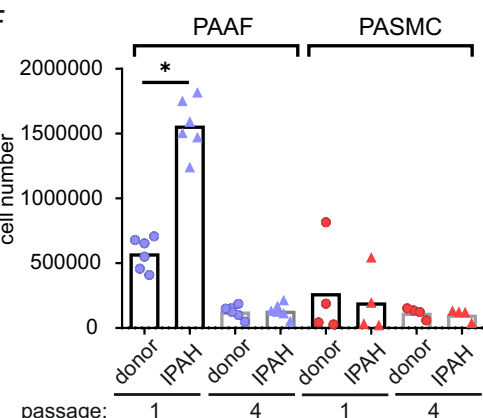
D



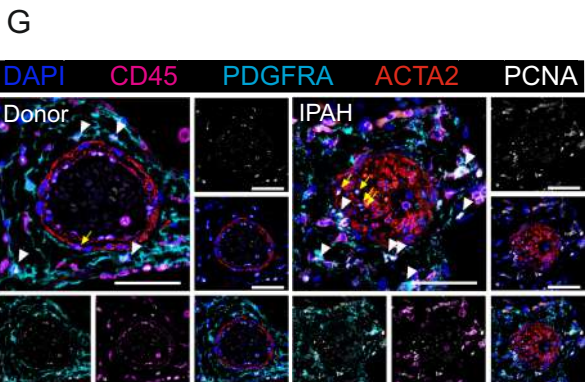
E



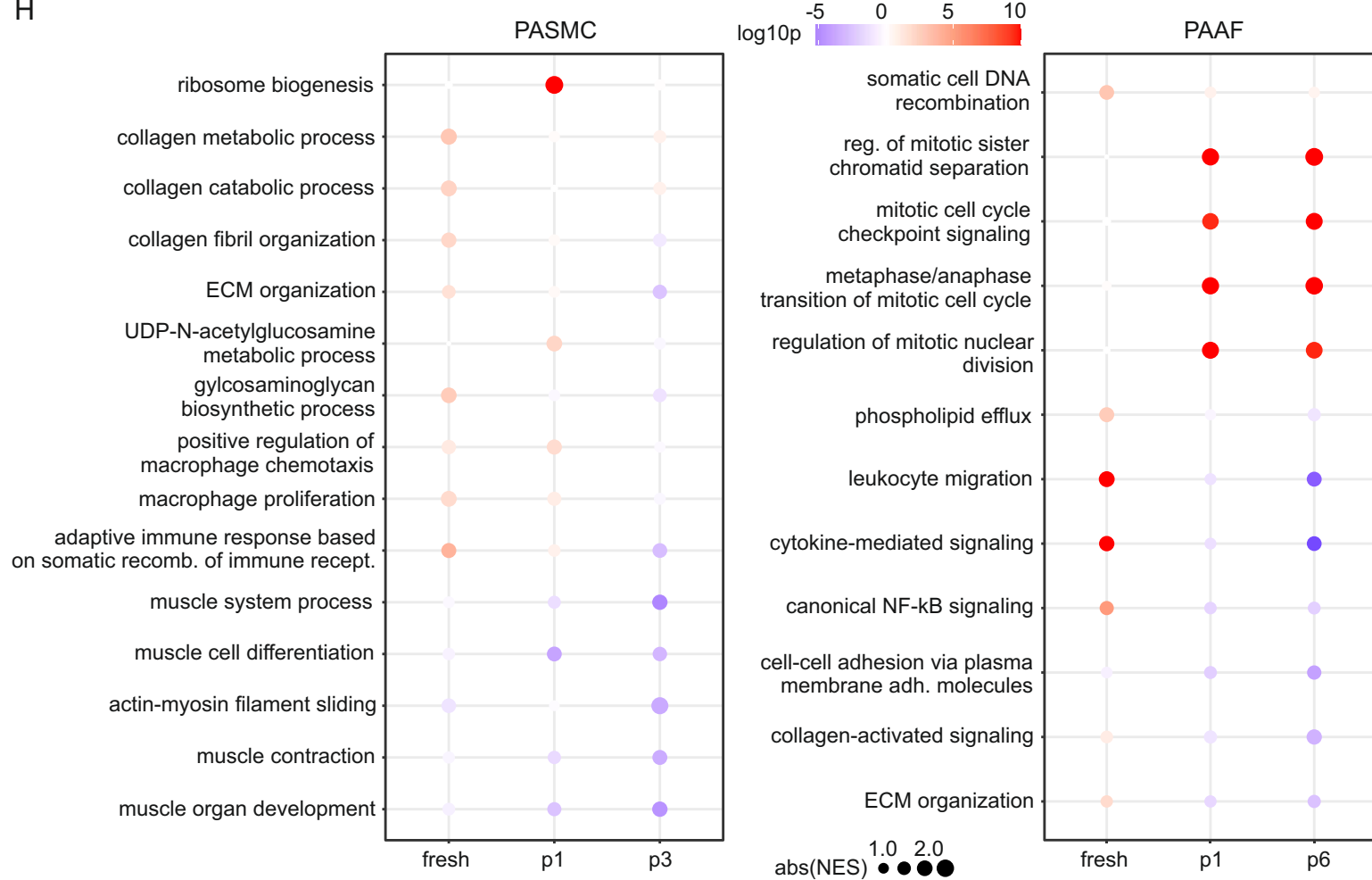
F



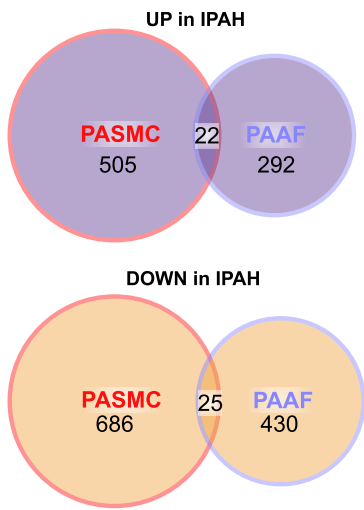
G



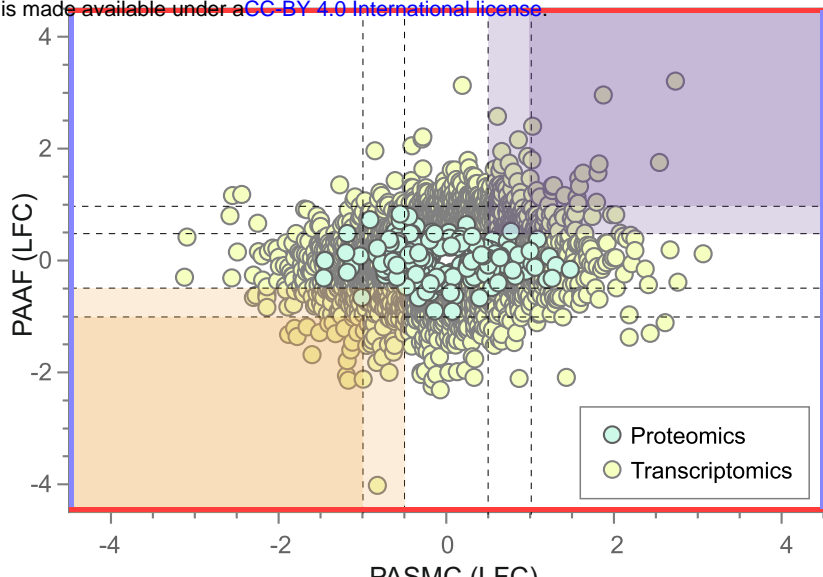
H



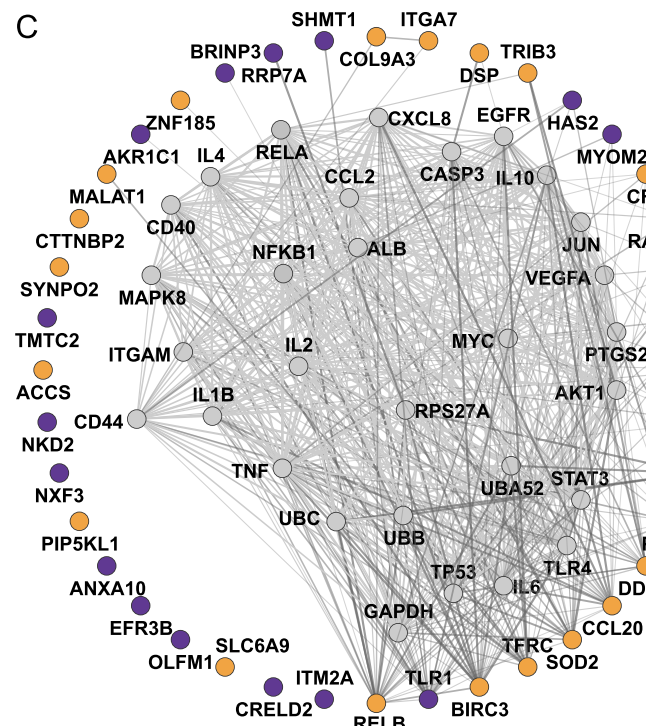
A



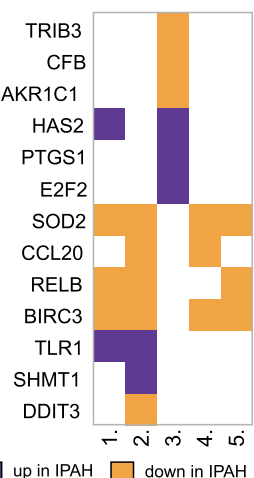
B



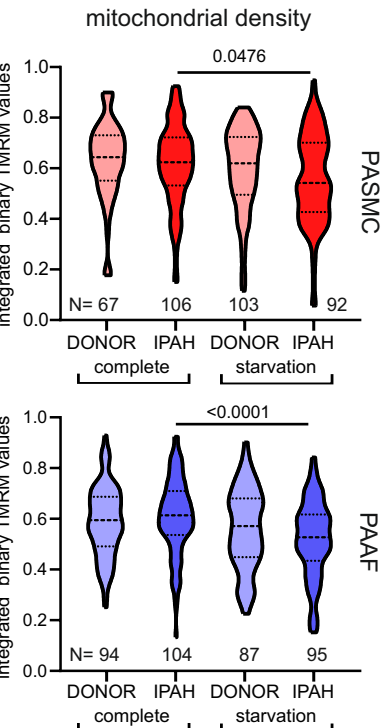
C



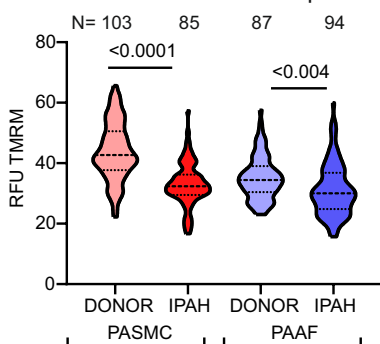
D



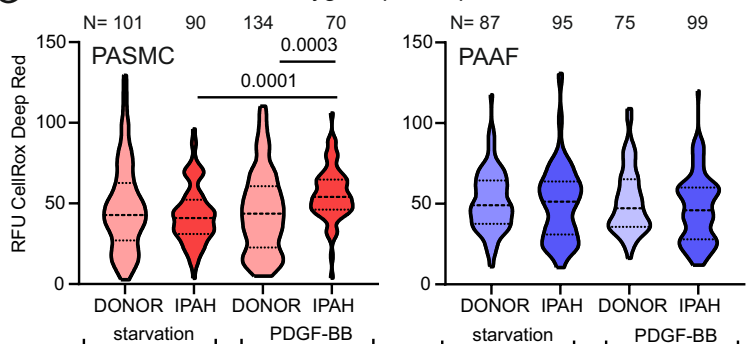
E



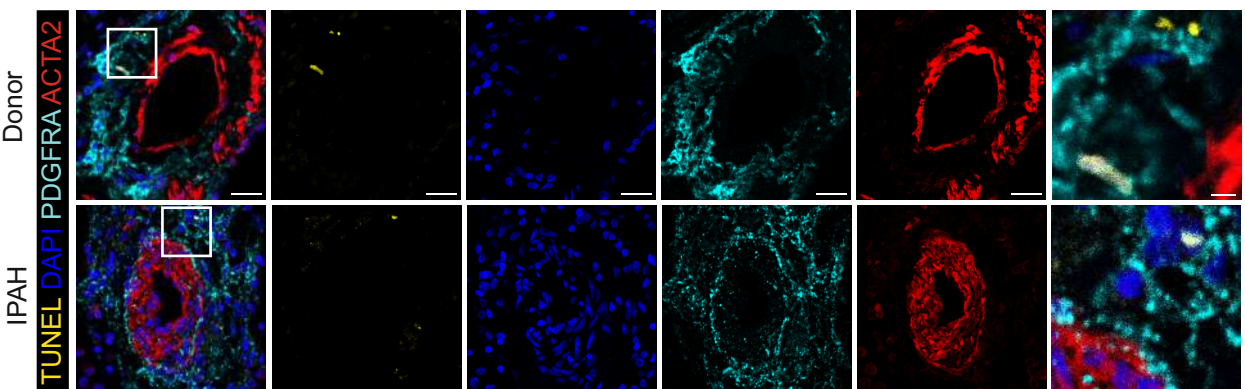
F mitochondrial membrane potential

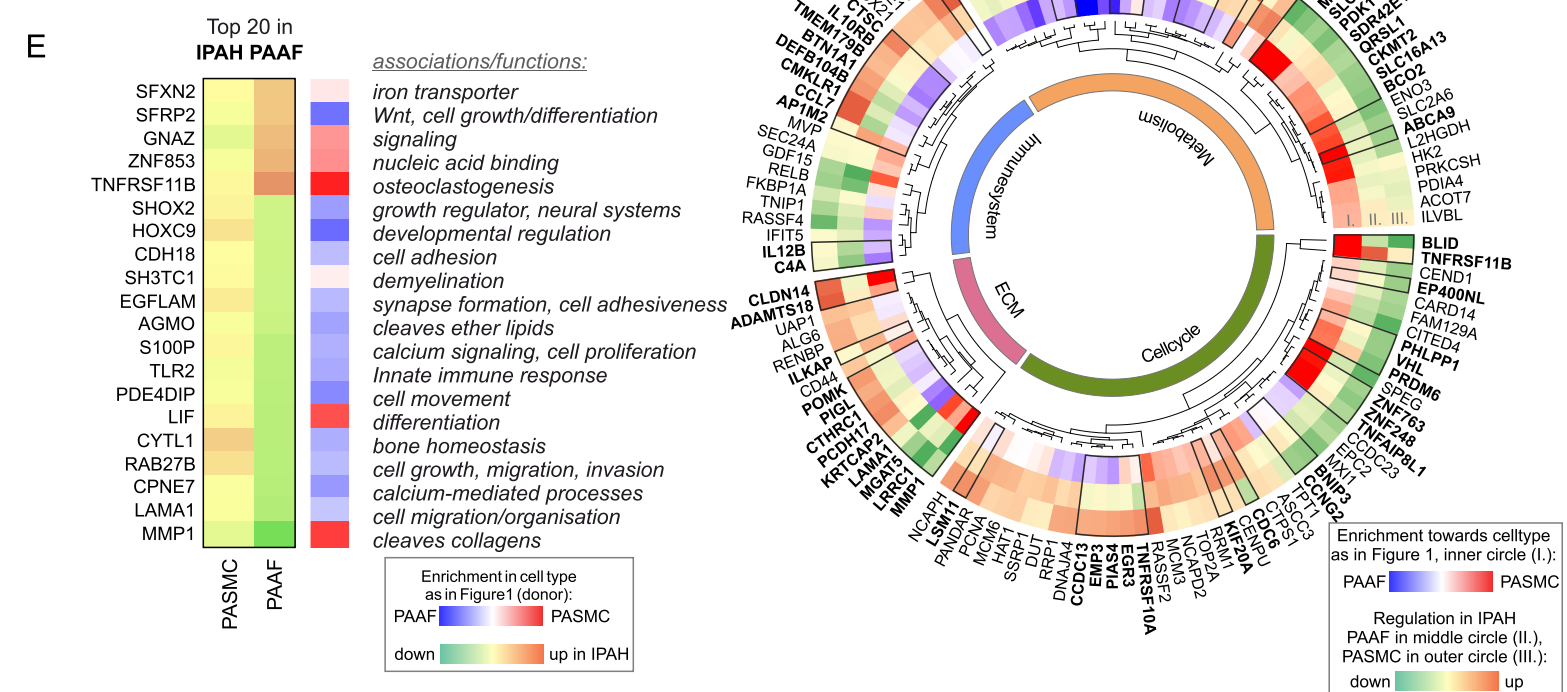
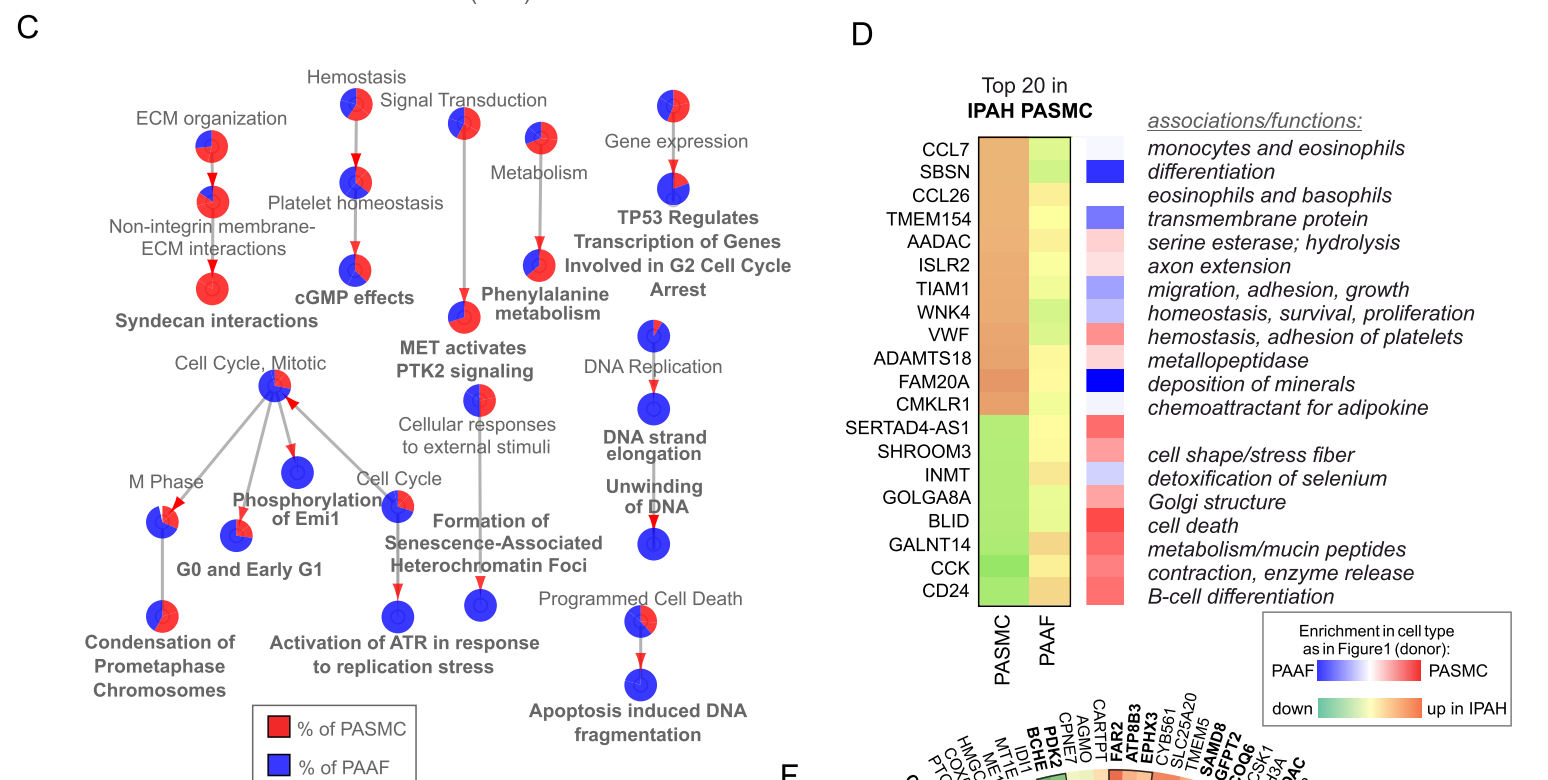
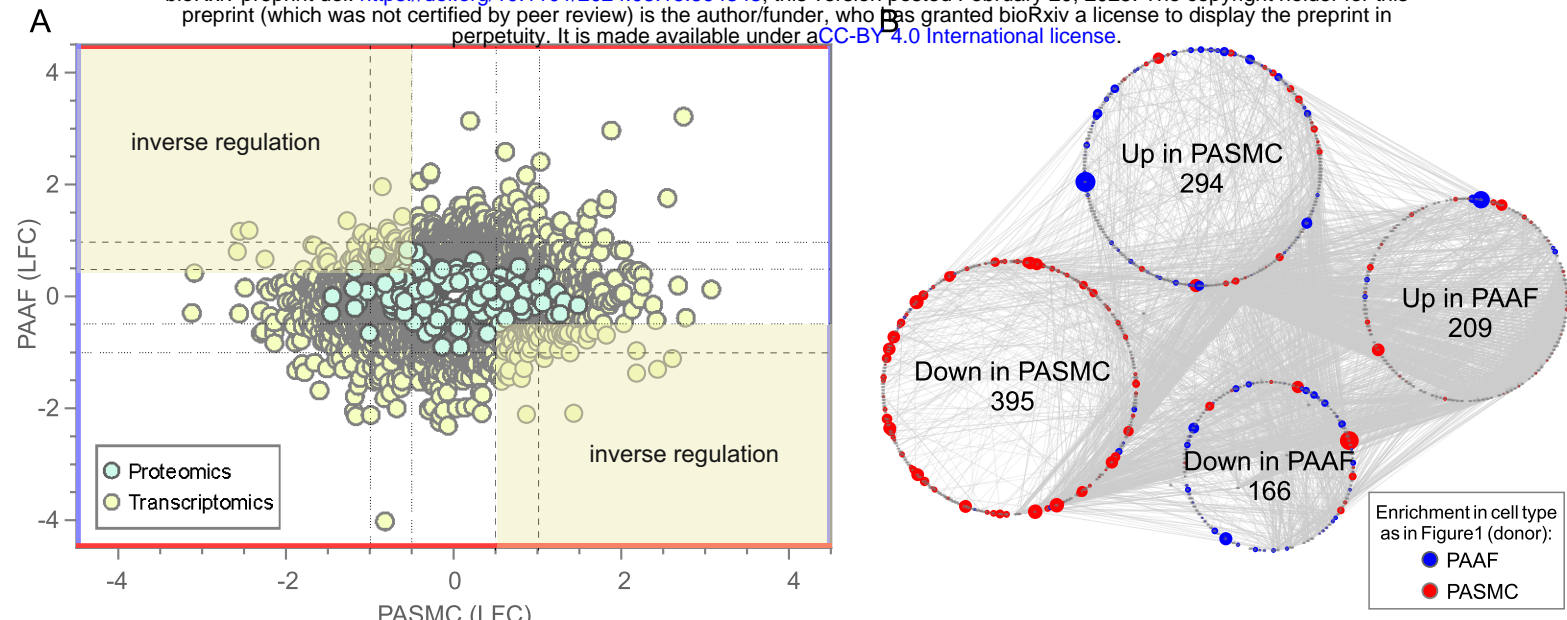


G reactive oxygen species production

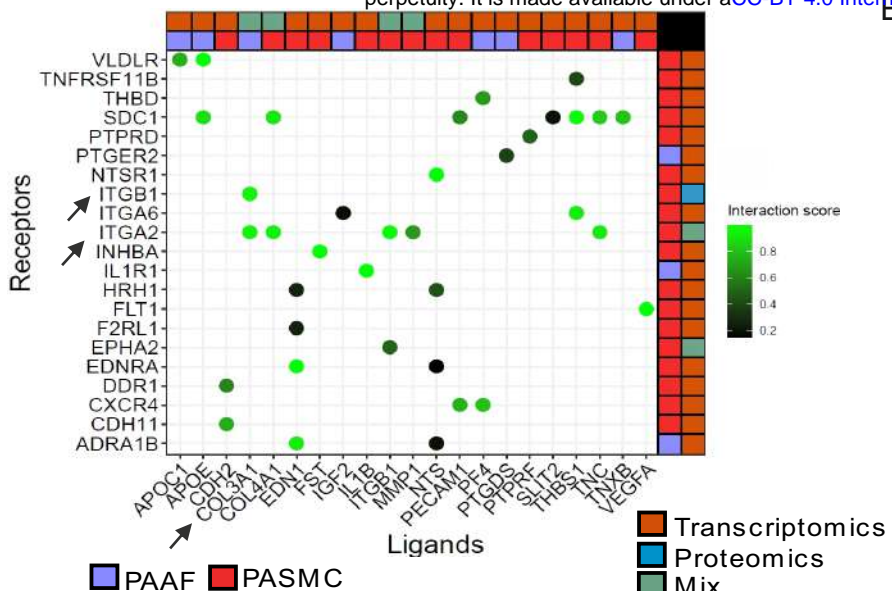


H

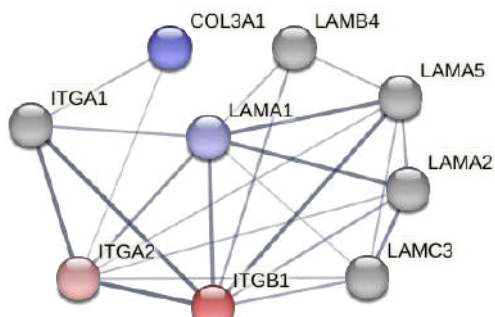




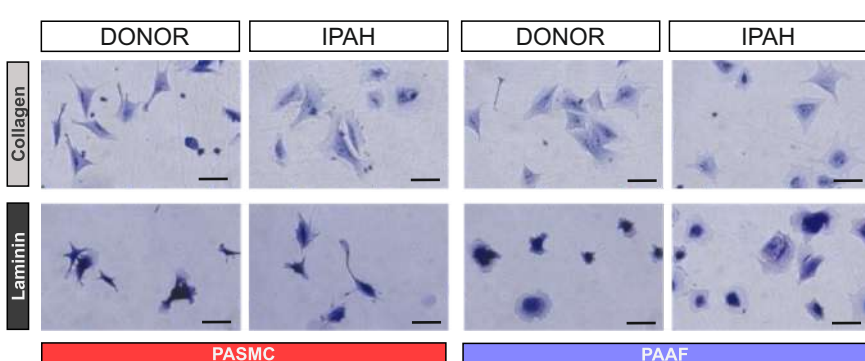
A



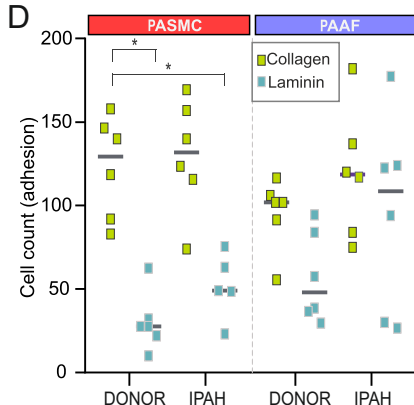
B



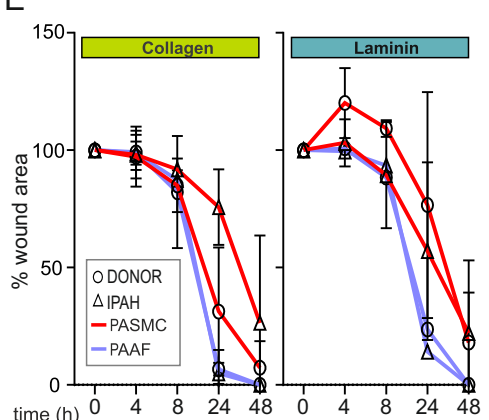
C



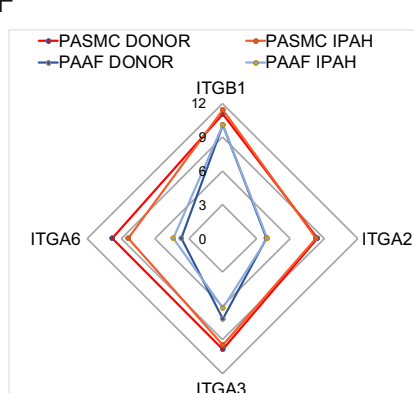
D



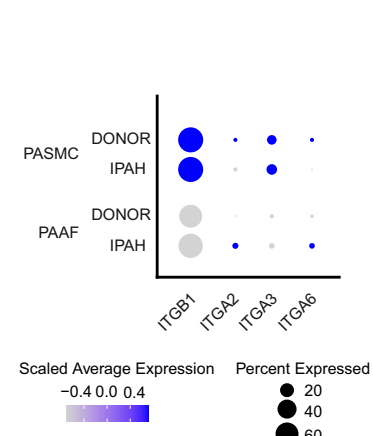
E



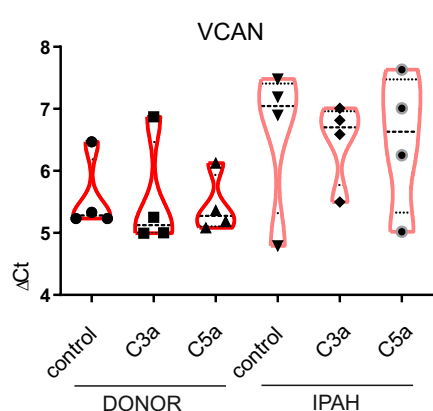
F



G



H



I

